PEER REVIEWED

Simulating Ar/He Plasma Sprays of Metal Particles

Alexander L. Brown[1] · Andrew Vackel[1]

Abstract A Lagrangian/Eulerian simulation technique for an argon/helium plasma spray including 10–100 micron metal particles has been developed and characterized for manufacturing applications including a unique equilibrium-based approach to the argon ionization problem. Six metals were studied for behavior under a characteristic flow condition to assess the sensitivity of model predictions for application purposes. Particular attention was paid to the thermal properties of the six candidate metals, and a number of uncertainties of varying significance were found in surveying existing source materials for the properties. Methods for determining injection boundary conditions based on measured nozzle parameters are exhibited. Spray dynamics have been affiliated with model properties, which may help guide the exercise of identifying optimal spray conditions for new applications. Particle-mean velocity and temperatures are compared to experimentally obtained data, suggesting the model provides a reasonable approximation of the nozzle dynamics at a low power setting. A number of uncertainties in the modeling characteristics of the nozzle are evaluated through a parametric evaluation. The exercise highlights the importance of input and boundary conditions to the accuracy of the resultant spray.

Keywords argon/helium plasma · Lagrangian transport · melt properties

✉ Alexander L. Brown
albrown@sandia.gov

Andrew Vackel
avackel@sandia.gov

[1] Sandia National Laboratories, PO Box 5800, Albuquerque, NM 87185-1135, USA

Introduction

Metal coatings applied by plasma spray can impart unique characteristics to engineered parts. The application of plasma sprays to problems of interest is complicated by the difficulty taking measurements in a plasma spray. The development of optimal operational conditions is challenged because one must deduce the correct settings that melt the metal particles so they will stick to the impacting substrate without adversely affecting (i.e., melting or deforming) the target and minimizing vaporization of the metal. Historically, our operations have largely been guided by empirical application of a variety of settings and conditions and using microscopy on the deposit to infer adequacy. This approach is not necessarily an efficient process and complicates the extension of the technology to problems with even slight variations outside the original test conditions.

Having a predictive model of the test condition can help to understand the dynamics of the plasma spray system and provide insights into the operational behavior. The use of modeling and simulation is a challenging problem due to the complexity of the physics involved in plasma sprays. Many computational fluid dynamics (CFD) packages use Eulerian-based solvers to simulate the Navier–Stokes equations for flow dynamics with a variety of approximations for sub-grid turbulent behavior. Adding an enthalpy equation permits thermal problem simulation. Lagrangian/Eulerian coupling is commonly used for simulating sub-grid-sized dilute sprays within a CFD simulation. Participating media radiation (PMR), plasma reactions, and multiphase evaporating drops round out the primary domain physics and computational capabilities that contribute to the behavior of the sprays.

Simulating particle-laden plasma sprays has been practiced by a number of groups as indicated by a review of the literature. It has been suggested that the initial modeling effort was that of Chang and Ramshaw (Ref 1), in which a 2D argon plasma jet was simulated employing a multi-state approximation for the ionization of the argon. Many other simulation studies followed and included a variety of emphases on different aspects of the problem including a variety of modeling techniques providing differing fidelity. An instructive way of representing the prior work is to categorize the published studies by research group, and by some characteristic assumptions. Table 1 lists the findings from the exercise and helps illustrate variations in historical simulation work. Use of argon or argon–hydrogen mixtures are the most common.

The zirconia sprays are most common, and most of the rest of the spray particle types have been documented in studies once, not multiple times. Fluent is the most widely used software, however, there are several other codes that have been used. The plasma is more often modeled with a local thermodynamic equilibrium assumption (LTE), which assumes that the ionization state of the medium is at thermodynamic equilibrium to simplify the gas-phase reaction modeling. Magneto-hydrodynamics (MHD)

involves the coupling of the fluid flow to the charge effects and is ascribed to studies including a form of the Maxwell equations interacting with the flow solver. The Chang and Ramshaw (Ref 1) multi-state approximation is unique to the group at Idaho National Lab (INL). A number of other significant variabilities exist among historical studies, including 2D and 3D assumptions, and turbulence model assumptions including Reynolds Averaging of the Navier–Stokes (RANS) approximations (normally the k-epsilon model or an extension thereof) and Large Eddy Simulation (LES) assumptions. LES is generally considered more accurate because it can better resolve the dynamics of transient behavior with added spatial resolution. RANS turbulence modeling continues to be relevant in this application space because it is generally more computationally efficient.

There are a large number of additional studies that are significant and often higher fidelity but lack either the computational aspect or the particle dynamics in tandem with the flow. Noted here are the reviews of Fauchais and Vardelle (Ref 22, 23), the review and property work of Murphy (Ref 24, 25) and Murphy and Urhlandt (Ref 26), the turbulence-centric study of Modirkhazeni and Trelles (Ref 27), the detailed torch studies of Lebouvier et al. (Ref

Table 1 Prior literature on simulation of plasma sprays with particle transport

Research group	Medium	Spray particles	Code	Plasma	Additional notes
Ahmed and Bergman (Ref 2)	Ar/H$_2$	Zirconia	Fluent	LTE	Simulated particle gradients and melt
Chang and Ramshaw Williamson et al. Xiong et al. (Ref 1, 3–5)	Ar, Ar/He	NiCrAlY	LAVA	Multi-state	2D initially, updated to 3D
Dalir et al. (Ref 6–8)	Ar	Zirconia/solvent	Fluent	LTE, MHD	Suspension plasma spraying
Delluc et al. (Ref 9)	Ar/H$_2$	Zirconia	Genmix	LTE	2D
Jabbari et al., Jadidi et al. (Ref 10, 11)	Ar/H$_2$	Ni/Methanol	Fluent	LTE	RANS
Remesh et al., Kang et al., Kang et al. (Ref 12–15)	Ar/H$_2$	Zirconia	Fluent	LTE	RANS; deposition patterns and angled substrates
Kanta et al. (Ref 16)	Ar/H$_2$	Alumina	Neural Network	Based on data	Non-isothermal particles
Kharlamov et al., (Ref 17)	Ar	Low carbon steel		LTE, MHD	Wire fed particle formation
Meillot et al. (Ref 18–20)	Ar/H$_2$	Molybdenum, Zirconia	Fluent, Aquilon		RANS and LES, some suspension injections
Pourang et al. (Ref 21)	Ar/H$_2$	Zirconia	Fluent	LTE	Studied deposition on curved surfaces

28), and Chazelas et al. (Ref 29), and the high-Mach number 2D work of Kaminska et al. (Ref 30). These represent a wider number of applications, code, media, etc.

We are focused on an experimental spray capability using argon–helium plasma. We seek to evaluate a number of metals for coating applications. These two aspects alone constitute unique model components based on the survey results in Table 1.

Activities involving selection of test conditions and particle assessments are done much more efficiently with a computational tool than using an empirical experimental approach. We have elected to conduct simulations with SIERRA/Fuego, a massively parallel generalized reacting flow low-Mach solver developed for fire modeling, but extensible to a number of other application areas. This decision was made mindful of the lack of plasma reaction capabilities and high-Mach capability in the code. Being a code internal to our lab, we benefit by being able to develop directly in the code base. Additionally, we leverage the historical verification work and optimize our ability to utilize the computational resources available (no imposed limitations on number of processors used). As activities ensued, it became clear that there was an historical lack of attention paid to a number of features of the particle dynamics. Specifically, the prior work tends to focus on a single particle type and as a consequence there is little focus on the general adequacy of the high-temperature properties to the resulting spray dynamics. Computational quality control also tends to be mixed, with mesh resolution studies, validation, and parameter variations tending to be the exception rather than the norm. This variable adherence to quality standards is also noted in the discussions of Modirkhazeni and Trelles (Ref 27). This comment is not intended to be a direct criticism of any particular contribution to the prior work, rather a general observation that the historical work can by virtue of focusing well on particular aspects of the challenging problem be lax in other aspects. There is a substantial amount of work needed on a variety of difficult problems before an ideal is realized that provides a general modeling capability applicable to all regimes of interest.

This paper describes an effort to simulate an Ar/He plasma spray for a variety of metals in an Ar environment. Methods are developed centric to the material properties to enable confident and credible predictions. As we mature our capability, we are identifying and filling in gaps in the process and procedures that help improve the ability to make both qualitatively and quantitatively accurate assessments of plasma spray processes. These will help enable a continuing improvement in modeling capabilities and should enable a more insightful and efficient application of plasma sprays to manufacturing efforts.

Methods

A process was followed in the setup of the simulations that was intended to add confidence to the material property aspects of the modeling. All property information was intended to be sourced to at least two independent references. This was to understand the variability in published properties and was motivated by an understanding of the challenges associated with obtaining properties, especially in the high-temperature regime. Given that rare or hard to obtain properties sometimes are sourced to a limited number of experiments, attention was paid not just to the values provided, but the sources referenced. The traditional approach to property determination is to source scientific literature values. These are peer-reviewed and backed by the reputation of the publishers. Web-based sources are generally considered less credible and subject to more variability in the rigor of the review. For this effort, a combination of approaches was of necessity required. This is partly because the properties needed can be difficult to find, and there is no single source for all the needed parameters.

Here the subsections introduce the simulation software, discuss the geometry of interest, the test conditions, the plasma model, the particle properties, and the particle distribution methods. We omit an extended discussion of the low-Mach number approximation other than to mention that despite simulating velocities as high as 600 m/s in this scenario that under atmospheric conditions would constitute high-Mach, the cases are deemed appropriately simulated with the low-Mach approximation. The speed of sound is functional with temperature, and the temperatures are high enough in this scenario where the velocities are high to render this potential problem less relevant due to the particulars of our experimental conditions. Conditions are low-Mach (i.e., $M < 0.3$). Under changing conditions, this assumption would need to be re-assessed.

This work focuses on six metals chosen due to their candidacy for our uses and for purposes of spanning a range of properties from high to low melt temperatures. The six selected metals (listed alphabetically) are aluminum, copper, molybdenum, nickel, niobium, and tantalum. This range of metals helps demonstrate the sensitivity of a spray condition to the metal being injected.

SIERRA/Fuego

We elect to perform simulations using SIERRA/Fuego. SIERRA is a framework developed at Sandia National Labs for a myriad of engineering science applications. Fuego is a sub-unit of the Fluid Mechanics branch that is focused on providing capability for predicting fire

scenarios. It is suited to the present application because it already has a number of capabilities that are focal requirements for simulating plasma sprays. The reacting flows capability, the turbulence models, the participating media radiation, and the evaporating Lagrangian particle spray model are all existing features that lend to the predictions at hand. Fuego is primarily differentiated from other computational fluid dynamics (CFD) tools by virtue of being designed using a control volume finite element method (CVFEM) instead of the more traditional control volume (CV) method. The SIERRA framework brings utility to leverage massively parallel capabilities on large clusters of compute nodes. More information on the equations solved, the implementation methods, and the capabilities are found in corresponding documentation (Ref 31, 32) as well as Appendix.

All simulations are run using the same version of the code, 4.5, 8.3, which assures repeatability of the simulations and leverages the nightly regression tests performed on the code for verification accuracy. Validation is normally considered to be a quantitative assessment of the accuracy of predictions and is pragmatically required for each application. We leverage to some extent historical validation work, but we are also seeking to add to the model validation, in particular, in model regimes or combinations that are historically lacking in prior characterization.

In this study, all the simulations are performed with the TFNS turbulence model that is a hybrid LES/RANS capability (Ref 33) with a filter width of 30 μs. The particle radiation is simulated using a fixed emissivity of the particles. Gas (participating media) radiation is neglected. This is informally justified based on the precipitous drop in volumetric radiative emissions approaching and below 10,000 K as per the computations of Meillot et al. (Ref 18) for Ar/H_2. Our scenario is believed to exhibit temperatures mostly lower than this exiting the nozzle, and replaces the radiating H2 with more transparent He, which may be assumed non-participating at these temperatures. The particle model largely follows the approach of Sirignano (Ref 34). Evaporation is governed by the Clausius–Clapeyron relationship. Particles lose heat by radiation, but the gas is assumed not to radiate. Visible observations of this scenario suggest an optically thin glow produced by the plasma gas. Particles are sub-integrated in a Lagrangian framework through the Eulerian CFD field. They are assumed isothermal in space, varying in time according to the interaction with the gas environment.

Experimental Test Conditions

The physical system that has been the basis for the modeling is the Controlled Atmosphere Plasma Spray (CAPS) system at Sandia. The system consists of a negative- and positive-pressure rated chamber with appropriate cooling, pluming feedthroughs, and robotics to conduct plasma operations in a pressure range from medium vacuum to slightly above atmospheric ($\sim$ 630 Torr or 84 kPa in Albuquerque, NM, USA) using Air, Nitrogen, or Argon. For the experimental work described herein, the chamber is evacuated to a base pressure of < 20 kPa (150 mTorr) and then backfilled with ultra-high purity Argon to 85.3 kPa (640 Torr). Pressure is regulated through a butterfly valve with feedback control to maintain a 85.3 kPa (640 Torr) pressure.

Plasma spraying was performed with a SG-100 torch using Argon and Helium plasma gases, using a standard 730/720 anode/cathode pairing and the 112 straight gas ring. Plasma gas flows were 21.5 and 3 slpm for Argon and Helium, respectively, and a torch current of 400 amp was used. The given experimental parameters use lower plasma gas flow rates and amperage than generally considered normal for the SG-100 and should not be considered optimized. However, the lower quenching power of an Argon atmosphere versus an air atmosphere allows the lower power spray condition to effectively melt metallic particles (Ref 35). Powder injection was external to the torch body and angled slightly downstream using SG-100 hardware and a powder gas flow of 1.2 slpm Argon. H.C. Starck Amperit 150.074 Ta powder was measured to be delivered at a rate of approximately 14 g/min. Measurements of the physical position of the injector for meshing were made using a caliper, with the injector orifice measured by viewing under scanning electron microscope.

Average torch voltage (V) and current (I) were used to calculate the gross power delivered to the SG-100 torch. Measurement of the torch's cooling water mass flow (M) and temperature differential after passing through the torch body (ΔT) was used with the heat capacity of water (C) to calculate the net power of the torch during operation as shown in Eq 1.

$$\text{Net Power} = (I \cdot V) - (M \cdot \Delta T \cdot C). \qquad \text{(Eq 1)}$$

This approach to the inflow boundary assumes that external losses like radiation and convection of the exterior surfaces of the nozzle are negligible. Average particle temperature and velocity measurements were made using the Accuraspray 4.0 (Tecnar, Saint-Bruno QC, Canada), which is capable of recording measurements at a maximum rate of one per second or be measured as a running average over several seconds. The specialized enclosure used to protect the Accuraspray from the CAPS environment and the SG-100 in operation are shown in Fig. 1. Velocities are deduced from transit times through the sample volume. Mean temperatures in the sample volume are deduced from a two-color pyrometry technique.
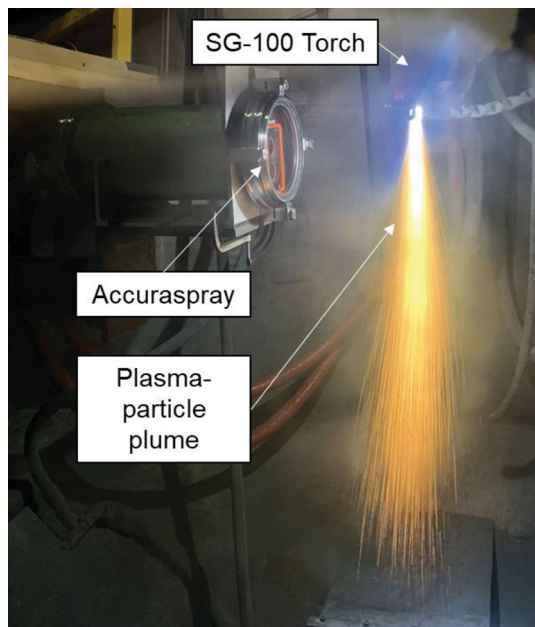
Fig. 1 An annotated photograph of the experimental setup

Table 2 Nominal test conditions for the plasma scenarios in this study

Operational condition	Value
Current (A)	400
Voltage (V)	24.2
Cooling water flow (l/min)	42.6
Cooling water temperature rise (°C)	1.83
Net power (kW)	4.24
Primary argon flow (SLPM)	21.5
Primary helium flow (SLPM)	3
Secondary (particle entrainment) argon flow (SLPM)	1.2

Test conditions are summarized in Table 2.

Mesh and Geometry

The geometry was deduced from caliper and micrometer-based measurements of the SG-100 nozzle, and the simulated geometry is described in the subsequent figures in this section. Figure 2 shows a cut-plane of the domain through the centerline shaded by contours of velocity and temperature from an instantaneous realization of the simulation at 0.1 s, which is a representative of a mature instantaneous prediction well past the start-up transient.

The nozzle was modeled in full 3D initially with both hexahedral and tetrahedral meshes. This effort is primarily concerned with simulations involving the hexahedral mesh. The domain was 8 cm diameter around the nozzle, and the spray was assumed downward with the end of the nozzle

being the zero point for the vertical z-coordinate. The domain extended 15 cm below the nozzle, with a wall boundary at the bottom, and open boundaries around the perimeter of the domain. For the tetrahedral mesh, a capillary tube (1.5 mm internal diameter, 4.78 mm outer diameter) was meshed through which the particles were introduced. The flow was modeled through the tube with particles adjusting to the motion of the gas due to drag. The hexahedral mesh did not include this feature, and simply introduced the particles at the end of the capillary tube with a velocity approximately consistent with the flow rate of the carrier gases (2.5 m/s). This is in part due to the challenge of producing a good quality conformal hexahedral mesh around the geometry while including the secondary inlet. An illustration of the baseline mesh resolutions is found in Fig. 3.

The hex mesh was constructed using a 'sweeping' operation that projects the top mesh downward. Resolution in the dynamic regions was in the range of 0.5 to 1.0 mm, with a gradual expansion biasing of the mesh in the z direction to 3 mm beginning below 10 cm beneath the nozzle. The exit of the capillary tube was 10 mm below the nozzle, and 9.75 mm away from the centerline with a downward angle of 13°. Given that the nominal mesh resolution in the nozzle was about 1 mm, the tetrahedral mesh required high resolution to simulate the internal flow. Both meshes were designed with a high focus of spatial resolution in the nozzle and below the nozzle to resolve the dynamics occurring as the plasma jet dissipates into the ambient chamber.

Plasma Model

In our case of an argon–helium plasma, we do not anticipate significant ionization of the helium until temperatures much higher than test conditions ($\sim$ 15,000 K) as indicated by Boulos et al. (Ref 36). The argon, however, ionizes at a lower temperature ($\sim$ 10,000 K), and exhibits equilibrium ion fractions of up to about 10% in the range of temperatures under consideration. This could be negligible, except the relatively large ionization energy of 15.759 eV, 1521 kJ/mol, or 38,000 kJ/kg (as per NIST Chem webbook) is a factor in determining the local gas temperature.

The dynamics of the plasma torch are largely assumed to occur in the torch, and the problem of solving the flow inside the torch would almost certainly demand a non-equilibrium model. The resulting stream of plasma is used as a thermal source to heat the particles and assumed evenly applied at the nozzle boundary. Videography supports this assumption, exhibiting minimal variability from the nozzle at these conditions. Particles may be injected through a port in the body of the injector, or outside the injector in a light gas stream. In the second case of an
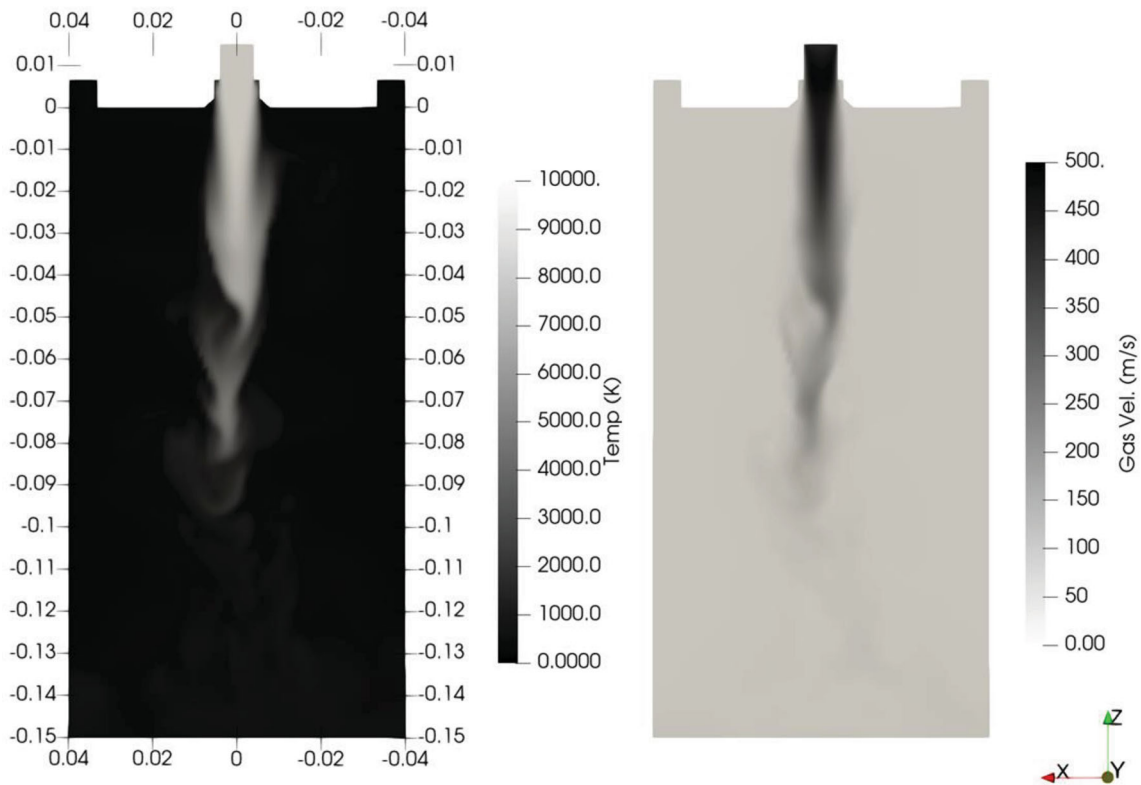
Fig. 2 Instantaneous predicted temperature (K) and gas velocity magnitude (m/s) with length scale annotated in meters
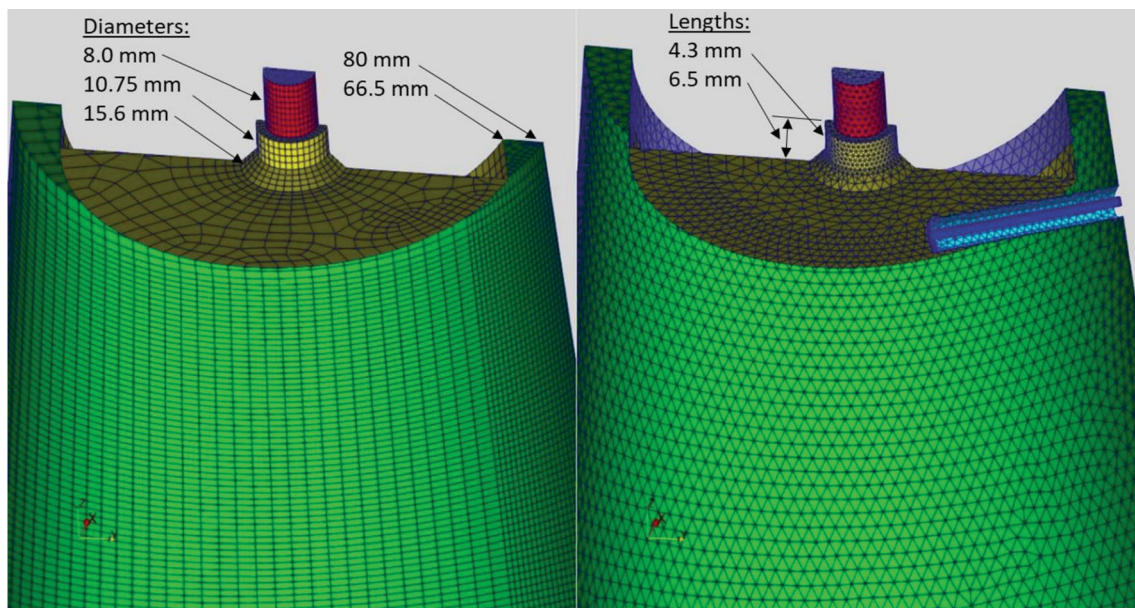

Fig. 3 An illustration of the computational meshes and SG-100 simulated dimensions

external injection, the plasma is not believed to be in a dynamic state, being away from the proximity of both the cathode and anode surfaces. The flow from the nozzle is in an open environment and transitioning back to a gas flow problem as the electrons and plasma ions re-combine.

Equilibrium codes minimize Gibbs free energy and simulate the species distribution for a given temperature/pressure combination. Assuming equilibrium-based concentrations of ions given the existing temperature could be a reasonable approach to the reactions of the gases
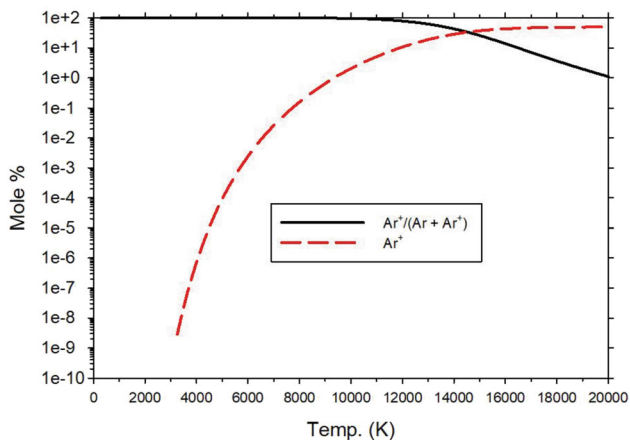
Fig. 4 TIGER predicted equilibrium argon and argon ion concentrations vs. temperature

Fig. 5 TIGER predicted molar fraction of ionized argon vs. temperature

depending on the conditions of the experiment. To implement this in our model, we employed the equilibrium code TIGER to create a tabulated dataset of equilibrium Argon and argon ion at one atmosphere pressure. TIGER was particularly well suited for this effort because it was developed for blast assessments and included previously characterized plasma-relevant equations of state germane to the high temperatures of this application (Ref 37). The simulation dataset is plotted in Fig. 4. This plot was verified to be consistent with a secondary source found in Boulos et al. (Ref 36).

These data are re-cast in terms of the Ar^+ fraction of total Ar ($f_{Ar} = Ar^+/(Ar + Ar^+)$) as shown in Fig. 5. This expression provides a convenient form for the model and the trend with respect to temperature. The functional shape has a trend that can be expected to be fit with some relatively simple functional models.

To use the equilibrium data in the code, an empirical function was fit to the TIGER data. This provided a simple means to access the equilibrium concentrations without having to resort to a call to the equilibrium calculator every time a value was needed. Two initial models were first explored employing the error function (erf) and the hyperbolic tangent (tanh) functions:

$$f(T) = 0.5 + 0.5 * \tanh\left(\frac{T}{C1} - C2\right) \tag{Eq 2}$$

$$f(T) = 0.5 + 0.5 * \text{erf}\left(\frac{T}{C1} - C2\right). \tag{Eq 3}$$

A parameter regression was used to generate fits, and the error (difference squared) was evaluated for each of the fits as a function of temperature. In this work, we elect to use the error function model in Eq 2 with constants C1 = 3277 and C2 = 4.4962. Additional model fits are explored in Appendix along with a more detailed accuracy assessment of the models.

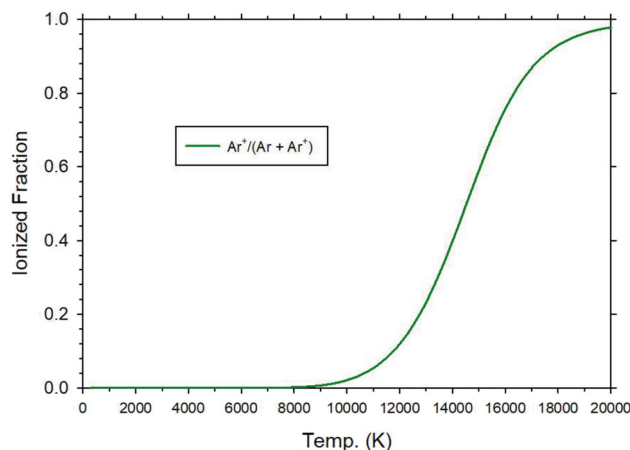The equilibrium approximation was implemented in our CFD code by defining a rate (k) to be related to the model function and the difference between it and the actual ionized fraction, fitting this general form:

$$k = C\left(f(T) - \frac{Ar^+}{Ar^+ + Ar}\right) \tag{Eq 4}$$

here C was to be selected such that the rate proceeded relatively fast without rendering unstable results. C was selected (after some trial and error) to be 50,000. The function is operationally intended to be one of the hyperbolic tangent or error functions, although could be any generic function. The model allows non-equilibrium results, but the further out of equilibrium, the greater the rate at which the reaction to restore equilibrium will proceed.

This method of treating the plasma respects the large heat of reaction in the argon ionization, and tracks the LTE assumption well, as suggestive of performance results described in Appendix. The heat of reaction (due to electron dissociation) is respected via the thermodynamic equations of state, which came from a standard NASA database and were verified to give the appropriate enthalpic shift. This method is believed to be as reasonable as LTE approximations for Ar and Ar/He plasmas for this application. To extend this to Ar/H2 plasmas, some adjustments for the ionization of the H2 would be necessary. Historical studies exist that suggest the LTE approximation may be lacking (e.g., Ref 1), but the studies purporting this tend to be limited to a specific set of conditions, and questionably valid for all applications.

A benefit to using this model is that it provides a convenient way to approximate the inflow boundary conditions for temperature and species. Having knowledge of the thermal loss to the sink by means of measurements of the inlet and outlet cooling water temperature and the flow rate

of the water, a net power to the plasma could be deduced by difference. This was used with knowledge of the specific heat of the inflow gases to identify the appropriate inflow temperature and plasma fraction of the inlet plasma spray, which could be expected to be accurate to that of the contributing measurements, thermal properties, minus the losses not accounted for otherwise (and assumed small at this point). This provides a direct link between experiments and the model, which is a significant asset given the difficulty associated with direct measurements of spray performance.

Using Eq 1, specifications from Table 2, and the plasma constitutive model detailed in this section, the average inflow boundary conditions representative of the test conditions were determined to be 0.648 g/s for the gas, at a temperature of 10059 K and corresponding equilibrium argon ion concentrations. A mass flow boundary condition was used for the main gas injector. The throat of the injector was also assumed at that same temperature, to not double count the energy lost to the nozzle. The rest of the body of the injector is assumed to be walls at 400 C. Measurements on the injector were lacking, but the temperature is constrained by the pre-test ambient and melting temperatures of the substrate and assumed otherwise minimally sensitive to this assumption. This provides an appropriate mean inflow condition for the gas exiting the nozzle, neglecting any transient behavior induced by the plasma dynamics in the nozzle.

Metal properties

During a successful plasma spray insertion, the particles undergo rapid heating through a phase transition from solid to liquid. Furthermore, they can evaporate, which accelerates as the liquid and/or environment temperature increases. Metal particles are relatively conductive, and since they are small may be assumed isothermal. This approximation is classically validated by performing a Biot number assessment that compares the rate of particle heating to the rate of internal transport. The Biot number is hL/k, where k is the thermal conductivity, L is a length scale, and h is the convective heat transfer coefficient. The isothermal assumption is best for scenarios with a Biot number significantly less than unity, and of diminishing validity with higher Biot numbers. Evaluation was made for some particles under typical conditions, and the analysis suggests the isothermal assumption may be reasonable. This assessment was complicated by the inaccessibility of detailed convective approximations for the particles during the dynamic phases, as well as the myriad of conditions possible through the dynamic response. Typical image analysis of deposits does not identify significant presence of shapes suggestive of transitional behavior (e.g., Ref 38).

The Biot number analysis alone is inadequate because it lacks accommodation for radiation effects and is very dynamic across the range of conditions for the process. The isothermal assumption has been a topic of study of some of the prior work (e.g., Ref 2, 16), but remains a point for further study with this work, as plasma jets vary significantly depending on inlet conditions. The assessment is specific to the plasma spray condition, particle types, gases, etc., and may need to be validated more rigorously in future work rather than reliance on the conclusions of prior studies and this simple approximation for a limited range of our materials and conditions. The SIERRA/Fuego implementation of the particle model largely follows the modeling methods described by Sirignano (Ref 34), which assess a particle temperature and a film temperature. The film temperature is much like a surface temperature, which we have found to be relatively similar to the particle temperature, more representative of an energy integrated average particle temperature.

To model the behavior of the particles, their properties need to be deduced. Based on a survey of typical conditions for testing, the plasma sprays of present interest involve temperatures varying from ambient up to perhaps as high as 15,000 K. Obtaining properties at ambient is relatively simple. Fewer labs can obtain information at very high temperatures. We have enlisted a variety of sources for thermal properties, and as a rule look to have redundant measures to confirm property values when possible. We also make effort to validate the properties obtained from publication sources compared with web-based sources. Some good information is obtained from the CRC Handbook of Materials Science (Ref 39), the ASM Thermal Properties Handbook (Ref 40), as well as webbook.nist.gov, engineeringtoolbox.com, periodictable.com, and efunda.com.[1] Additional (confirmatory) sources include heat transport textbooks, and journal articles. The NIST webbook and the Smithells Metals Reference Book (Ref 41 and older) were valuable resources, and were among the most detailed, being the prime sources describing in functional form the temperature dependence of the heat capacity of the solid metals. Properties required to perform the transport calculations include:

(1) Density (or specific gravity)
(2) Heat capacity
(3) Thermal conductivity
(4) Melting temperature

---

[1] https://webbook.nist.gov/chemistry/; accessed April and October 2020 https://periodictable.com/Properties/A/VaporizationHeat.an.html; accessed April and October 2020 https://www.efunda.com/materials/elements/element_list.cfm; Accessed October 2020 https://www.engineeringtoolbox.com/fusion-heat-metals-d_1266.html; Accessed March 2020.

(5) Latent heat of fusion
(6) Boiling temperature
(7) Heat of evaporation
(8) Critical temperature
(9) Atomic weight (to convert between moles and mass)

Heats of evaporation and fusion as well as phase transition temperatures and critical temperatures are scalars and not presumed functional with any important variables in this problem. The density, heat capacity, and thermal conductivity are a function of temperature. The density is subtly functional due to thermal expansion, and this effect is neglected. The heat capacity and thermal conductivity have a functionality with temperature that may be important, but since thermal conductivity is not used in an isothermal calculation we have not focused on this relation at this point.

An instructive outcome of this material property exercise was a better appreciation for the variability that exists in published property values. Two examples involving specific heat of two of our six selected metals are highlighted here. First, the specific heat of molybdenum as a function of temperature was found in two primary sources, which give appreciably different results. We initially were looking at ASM polynomials and found that the NIST values were substantially different once plotted on consistent unit basis. A careful read of the ASM documentation suggests properties originated from Smithell, which was an older version of the reference. Finding a copy of the newer handbook, we found the disagreement to be persistent. Figure 5 shows the specific heat data from references for molybdenum. All data sources agree near ambient conditions. At elevated temperatures, the deviation is marked. The Smithell polynomial is qualified to a range below the melt temperature and is not extrapolated in this plot. The Smithell documentation cites Hultgren et al. (Ref 42) as the data source for the polynomials. The source
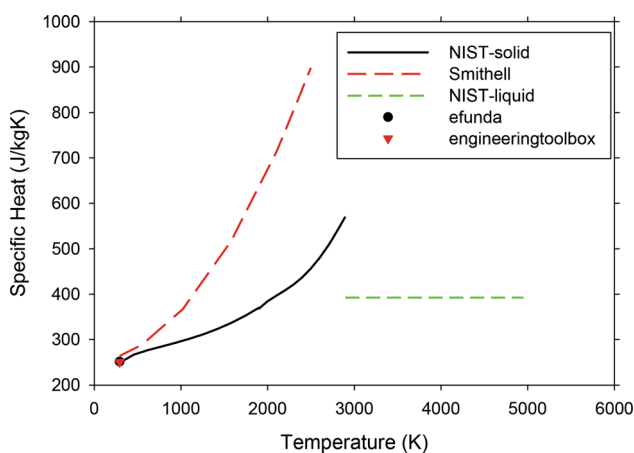
documentation aligns more closely with the NIST fit, which suggests an error in the polynomials from the Smithell source (Fig. 6). Hultgren et al. (Ref 42) also provide a detailed indication of data uncertainties, which are considerably smaller than the error differences indicated in Fig. 7, and suggests the tabulated data are consistent with a variety of prior measurements from different research groups.

Another case study involves nickel. The specific metal differs from the others in the study because it undergoes a solid phase transition from α to β states between ambient and melt temperatures. Both the NIST and Smithell polynomials identify this transition, however, the NIST fit involves three polynomials and a continuous transition between the states. The Smithell fit includes two polynomials, and a step function between the states. The NIST polynomial results in a significant, albeit temporary deviation from the equivalent trends from Smithell. This is seen in Fig. 6 and is more reflective of the agreement found for most of the evaluated metals.

Besides the differences in Ni and Mo, the specific heat for Nb diverged to about 40% difference from 2000 K up to melt. The specified validity range for properties of Nb from Smithell was up to 1900 K where the deviation begins. The NIST data are expressed as valid in this extended range, representing a suspectedly more reliable approximation for current modeling purposes.

Because the energy conservation is managed in the models by tracking particle temperatures instead of enthalpy, the latent heat model required modification to assure the particle dynamics were respective of the property. Each particle is integrated for Lagrangian motion and energy changes at sub-steps for each global Eulerian iteration. The latent heat was initially applied by including it as an addition to the specific heat across a 10° range at and just below the melt temperature. Evaluations of the results suggested that
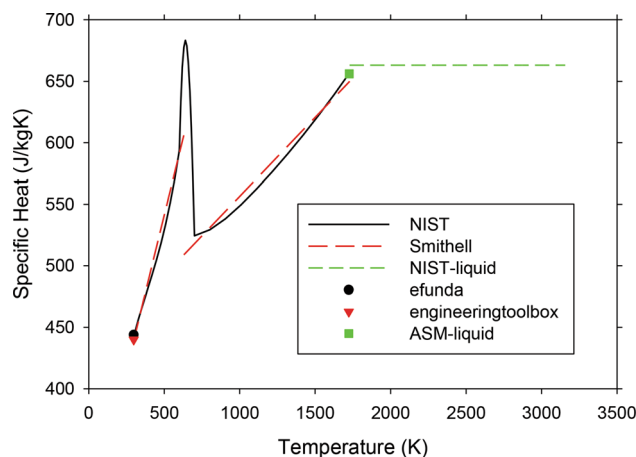

Fig. 6 Specific heat data for Mo from various sources

Fig. 7 Specific heat data for Ni from various sources

some particles were heating fast and stepping over the latent heat application range. Expanding this from

10 to 100°, we were able to verify that particles were step-integrated through this range and consequently achieving a more representative enthalpy behaviors simulating the latent heat of melt/fusion.

Implementing the specific heat polynomials required unit conversion, and manual entry of a large number of polynomial coefficients. To mitigate the likely potential for an error in this process, both the NIST- and Smithell-based specific heat models were expressed in a SIERRA input file that uses a function parser to deploy the functional relation during calculations. The same input line was directly copied into a gnuplot script, which was then used to plot the product relations for the Smithell and NIST-based models in tandem for each metal. An example of this comparison for Nb is found in Fig. 8, which illustrates the application of the aforementioned latent heat model as well as the differences between the two models for the specific heat of Nb approaching the melt temperature.

Additional variabilities in properties were found in the literature survey, but as they were of a more subtle difference, the details are included in Appendix.

Particle Distribution

There is an inherent distribution to particles whether based on a manufacturing process or a size selection process intended to generate uniformity. Particle size distribution of the Tantalum powder tested for this effort was measured using a Beckman-Coulter laser scattering particle size analyzer and is given in Fig. 9. The particle size distribution indicates particles outside of the nominally 15 to 45 μm size range, including a tail of fines. A scanning electron micrograph of a powder sample in Fig. 9 shows the non-spherical morphology of the powder and several fine (< 15 μm) particles. Since the laser scattering method
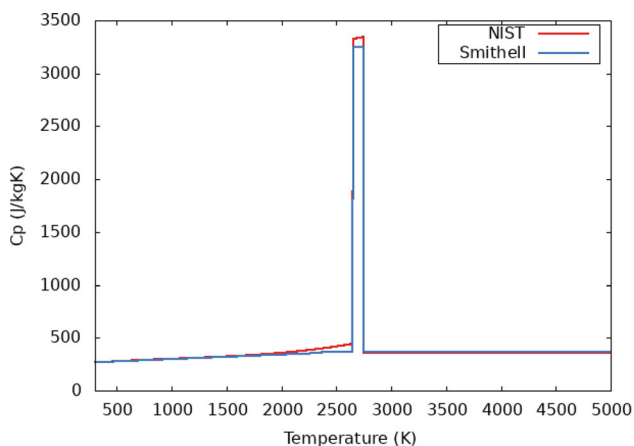
assumes a spherical particle for size calculation, it is likely that the non-spherical morphology gives a particle size distribution that includes particles larger than the 45 μm upper bound. We assume particles are spherical in the model, however, actual particles are shown here to vary somewhat from spherical.

The Weibull or also known as the Rosin–Rammler distribution is often used to characterize particle size distributions. We elected to abstract the distribution of the tests with a distribution of this nature. The relation for the probability distribution function (PDF) of this distribution is defined by:

$$f(d) = \frac{k}{\lambda} \left(\frac{d}{\lambda}\right)^{k-1} e^{-(d/\lambda)^k} \qquad \text{(Eq 4)}$$

here d is the particle diameter, and k and λ are distribution constants.

Using distribution parameters of $k=4$ and $\lambda=43$, a mean of 39 microns is predicted, with a corresponding number-based PDF and cumulative distribution function (CDF) shown in Fig. 10. The distribution is sampled to generate a time series of particles introduced at the nozzle exit with a velocity that resulted in entrainment of most of the particles for these simulations.

Results and Discussion

The simulations can be employed to explore the significant difference the metal has on the resultant melt of the particles at various heights. Parts for coating in practice are normally located in the range of 10-15 cm below the nozzle. This was largely empirically determined. Having simulation results helps better understand the dynamics occurring in that regime. We assume a consistent plasma inlet, as well as a uniform and equivalent particle size distribution for the injected particles. In each case, plots are sub-sampled from the actual simulations to omit a large fraction of the actual predicted particle instances. The sampling was initiated beyond 10 ms, after the start-up transient had completed. As particles are introduced in the flow about 1 cm below the nozzle exit, they flow into the hot jet where they rapidly increase in temperature and are accelerated downward by the fast jet. The average gas temperature cools further down in the stream by diffusion and advection. At some point in the flow, the gas continues to cool below the average temperature of the particles, and then the particles due to their thermal inertia are able to stay in the melt regime while the gases are cooling below that point. This is a relatively ideal spot for applying the coating, as the convective heating of the part is reduced from the comparatively cooler gas, and the particles may

Fig. 8 Specific heat model implementation verification plot for Nb
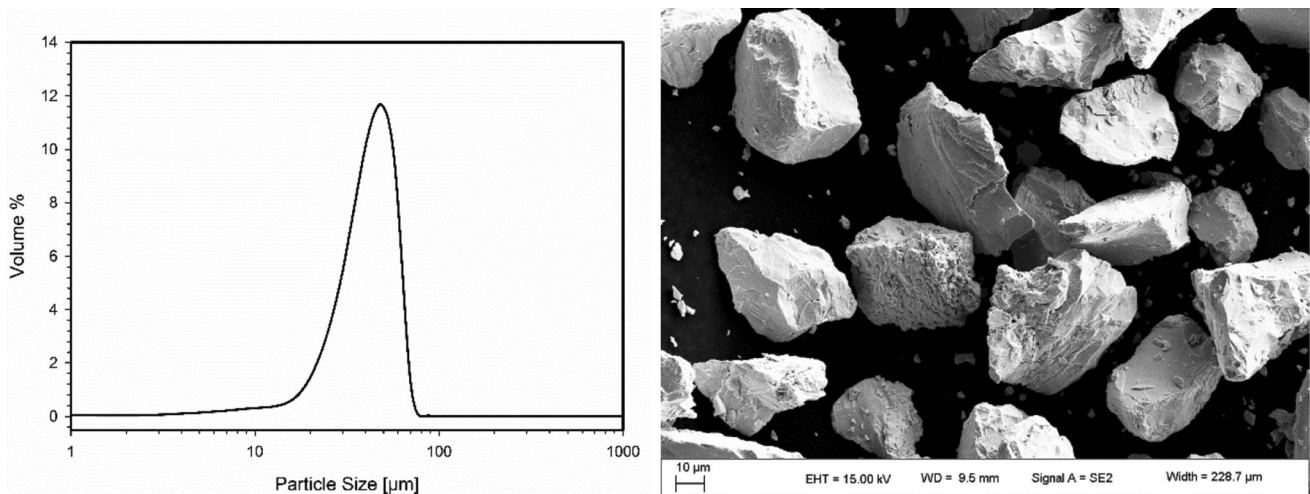
Fig. 9 A measured size distribution for particles (left) and a typical micrograph of Ta particles (right)
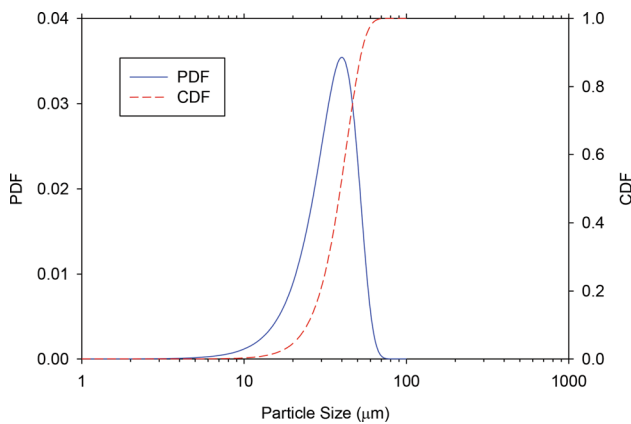

Fig. 10 The assumed particle distribution for simulations

still be sufficiently hot to be melted and to impact as a liquid onto the deposition surface and stick.

Present simulations neglect the presence of the part. We assume the part will have minimal effect on the dynamics of the spray above the part, and that the metal particles can be assumed to impact at approximately the conditions (i.e., temperature and melt) as are predicted in the free stream.

Mesh Refinement Evaluation

Results here will be illustrated for a consistent injection case. The inflow velocity and temperature are deduced from the power setting and the cooling water flow as detailed earlier. Our baseline ($\approx$ 1 mm resolution designated as 'medium') mesh results for centerplane velocity and temperature are shown in Fig. 11 with a comparable fine mesh ($\approx$ 0.5 mm) prediction to illustrate the minimal effect of refinement on the mean parameters of the centerline flow. Mesh refinement was achieved by a 2:1 split of

all hex edges, resulting in a mesh of about a factor of 2^3 greater control volumes. The averages were taken from 0.02 to 0.1 seconds. Figure 11 shows the temperature is similar throughout the flow, with a minor departure at in the $-$ 0.04 m range. This is where the flow begins to separate in the turbulent transition regime and is possibly suggestive of differences due to the added resolution contributing to additional dynamics in this region. By $-$ 0.05 m the results trend similar again and do so until the end of the domain. Velocities in Fig. 11 show a consistent decay of the velocity as the flow exits the nozzle. Upon exiting the nozzle at

0.0 m vertical position, the average jet flow steadily decelerates to about 100 m/s at -0.05 m where the rate of decrease shifts lower. Simulation results are similar for both resolutions, with some minor differences attributable to noise in the accumulation of the average. Average particle velocities and temperatures for a Ni injection are within 100 K and 5 m/s of each other for the two meshes across all heights, with the coarser mesh typically resulting in slightly higher temperatures and velocities.

One can see that at 10-15 cm below the nozzle, the average velocity and temperature have significantly decreased, both of which help reduce the potential for melting a part as it is introduced into the jet for coating.

There were additional preliminary mesh exercises performed with a wider range of element types (tetrahedral) including a wider range of sizes. Based on that analysis and including the plots shown here, we have confidence that we are in a regime of relatively small change based on added mesh. The baseline mesh had a nominal resolution of 1 mm in the jet, with significant relaxation away from the dynamic region. This facilitated simulation turn-around,
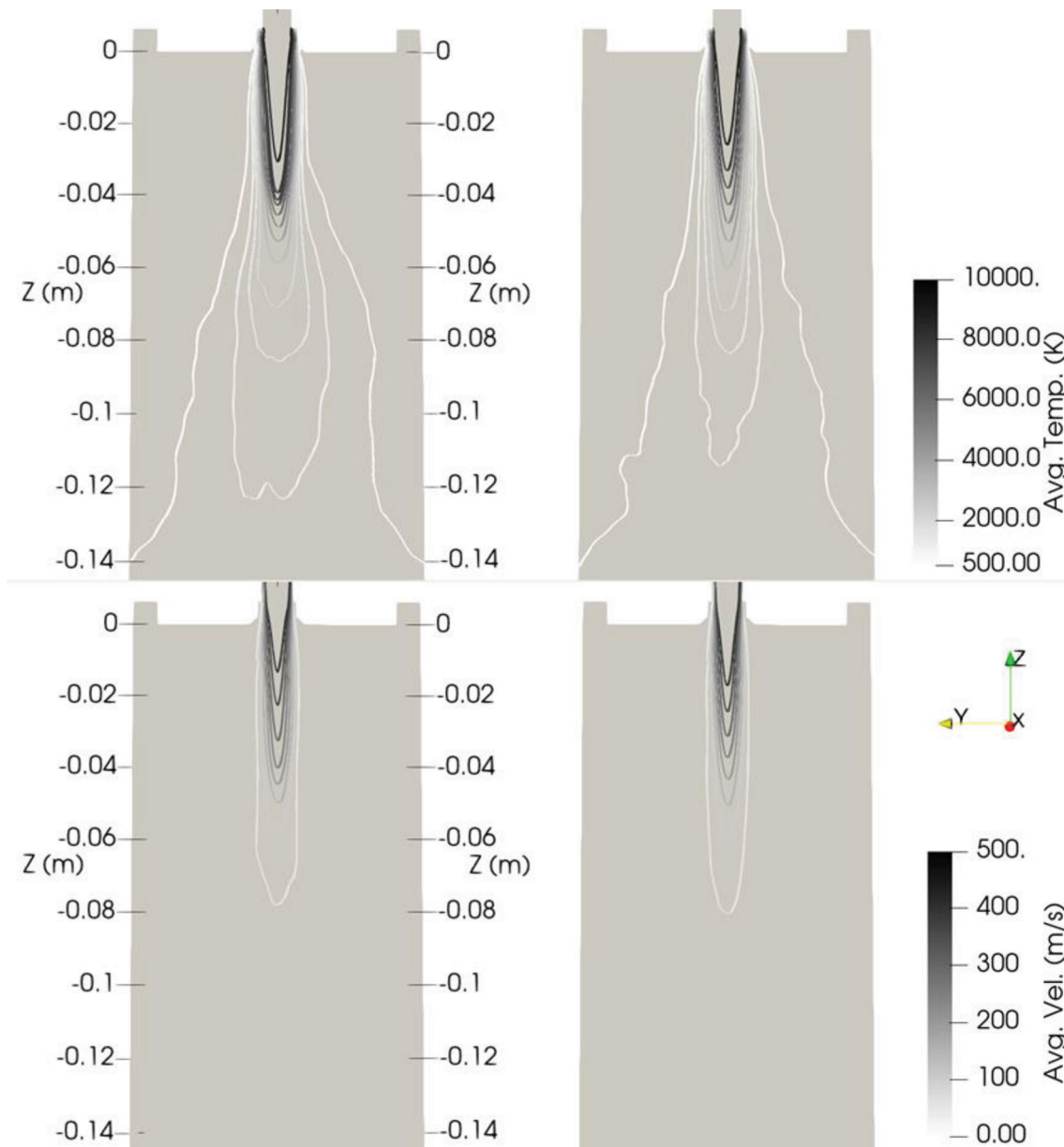
Fig. 11 Average centerline gas temperature (top) and velocity magnitude (bottom) comparison for the medium (left) and fine (right) meshes. Contour levels for temperature are 500, 1000, 1500, 2000, then increasing to 8000 by 1000 K. Contour levels for velocity are 50 m/s increasing by 50 m/s to 400 m/s

requiring hundreds of CPU days instead of thousands for the finer simulations.

Predicted Particle Dynamics

The particles are introduced at about 1 cm below the nozzle off-centerline toward the jet, and heat rapidly as they interact with the plasma jet. Coating quality is dependent on the particles remaining in the melt state so they deform and stick on impact with the substrate. We have elected to show results that illustrate the wide range of response of the particles by including three particle size ranges sampled across the assumed distribution. In each of the plots, the melt temperature range is obvious due to the clustering of the particle in that range, and also indicated by a dashed gray line.

Figure 12 shows the predicted particle dynamics for all the metals, with Aluminum in the upper left. Of the selected metals, aluminum has the lowest melt temperature. The particles are easily melted and are mostly well above the melt temperature in the 10-15 cm range below the nozzle. Some particles are over 1000 K above the melt
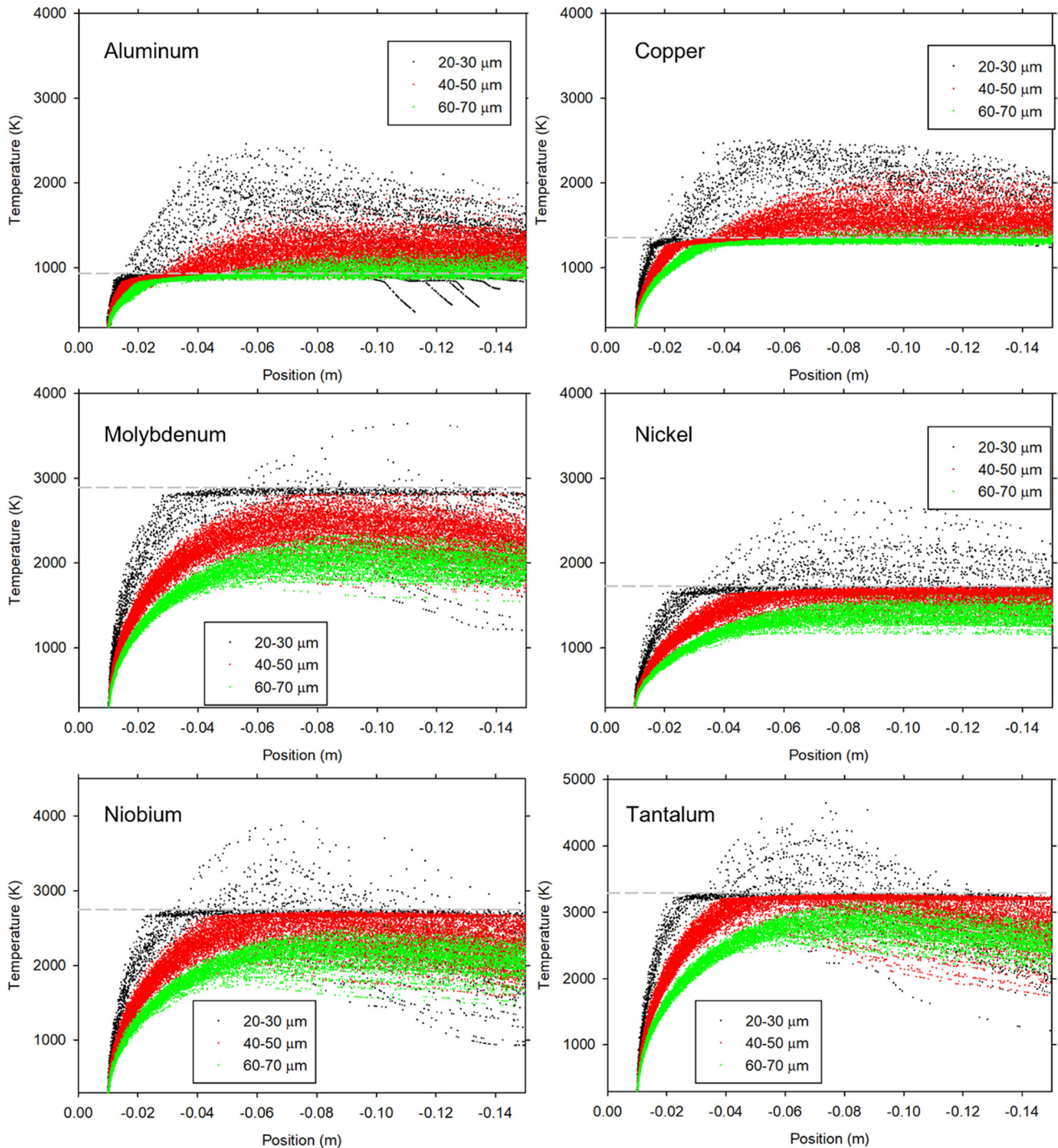
Fig. 12 Predicted particle temperatures for the six metals in particle sizes ranging from 20 to 30 μm (black), 40 to 50 μm (red or darker gray), and 60 to 70 μm (green or lighter gray) with reference melt temperature as a dashed gray line. Position is the vertical height with the nozzle exit as the reference zero (Color figure online)

temperature. This result is an example of a case where the injection conditions are possibly too hot for the given metal, as one would anticipate significant evaporation. Some of the smallest particles in the 20-30 micron range in the downstream cool much faster, and are below the melt temperature. This behavior is due to the combination of density and heat capacity, and these particles will likely not adhere. It also relates to the density, as the particles have less inertia compared to denser metals. Separate examination of the predicted particle sizes as a function of height

suggests there is little change in the particle sizes (< 1% maximum) even though they are evaporating and heating well above the melt temperature (not illustrated with a figure here).

Figure 12 shows similar results for copper in the upper-right. This is also a relatively low melt temperature metal, and the results are relatively similar to that of aluminum. The majority of the particles are at or above the melt regime after 3 cm below the nozzle. Smaller particles stay in the melt regime through the domain. This might be considered a case where adhesion potential is in the vicinity of being maximized for the particles across the range of the distribution.

Figure 12 shows predicted results for molybdenum in the middle-left using the NIST model for specific heat. The 60-70-micron-sized particles do not reach the melt temperature. These would be expected to bounce off the impacted substrate. Some of the 40-50- and 20-30-micron-sized particles are in the melt transition, and may adhere. Based on the results of this assessment, a higher temperature would be needed to achieve a higher probability of particle adhesion for this metal.

Figure 12 shows temperature results for the nickel particles in the middle-right. The specific heat model used was based on the Smithell data, selected because it involved fewer terms to compute the polynomial fit while giving similar accuracy to the NIST model. Some of the 20-30 micron particles are above the melt temperature range, suggesting the possibility of good adhesion. Many of the 40-50 micron particles are in the melt region, where they would be questionably adhered to the substrate. A small increase in the nozzle injection temperature would probably help achieve a higher fraction of these particles adhering to the substrate on impact.

Niobium injection simulation results are found in Fig. 12 in the lower-left. Many of the 20-30 and 40-50 micron drops reach the melt temperature range. Some of the 40-50 micron drops never reach this point, and none of the 60-70 micron particles appear to. For this metal, a higher temperature might be recommended, or a slightly smaller range of particle sizes.

The tantalum particle results are shown in Fig. 12 in the lower-right. Most of the 20-30 and 40-50 micron particles reach the melt temperature, while few in the 60-70 micron range do at 10 cm downstream. Some in the 20-30 micron range are above the melt temperature, and should stick upon impact. However, most of the larger particles are transitioning away from the melt range and are unlikely to stick. An increased temperature of the injector would be desirable here as well.

An instructive way of assessing the relative intensity needed from the plasma torch for a given metal is to calculate the energy required to heat from ambient to melt temperature (E_m). This may be calculated using this relation:

$$E_m = p\left[\left(\int_{T_a}^{T_m} C_p dt\right) + H_m\right] \qquad (Eq\ 5)$$

here C_P is the specific heat, T_m is the melt temperature, T_a is the ambient temperature, and H_m is the latent heat of fusion (or melt). Assuming a linear specific heat, a two-point integration can be used to approximate the integral term with the specific heat at the ambient and melt conditions. Using this method, the parameters in Table 2 show a consistent story with the prior figures. Molybdenum has the highest E_m, while aluminum has the lowest, followed by copper. The other three metals have fairly similar values in magnitude and might be amenable to spray applications under similar nozzle settings. The aluminum and copper would necessitate a lower setting, while the molybdenum would necessitate a higher setting. Also shown in Table 3 is the ratio of $\rho H_m/E_m$, which is suggestive of the fraction of latent heat energy required to achieve melt relative to the total energy to heat from ambient to melt. These parameters vary from 0.23 up to 0.37, suggestive of a variable role of the latent heat in the relationship.

Note also that the melt temperature, while a good indicator of the need for an increased setting on the nozzle, is an imperfect predictor. Tantalum has the highest melt temperature, yet molybdenum has a higher melt energy (Em) because of the large specific heat and latent heat of melt. Aluminum, with the lowest melt temperature, is still the lowest, but not by nearly as much as might be expected due to the relatively large specific heat and latent heat of melt. Nickel, with a comparatively low melt temperature, ranks similar to niobium with a melt temperature about 1000 K higher. Indeed, their particle traces presented earlier are relatively similar, differing especially at the low particle sizes. The differences are probably attributable to a combination of factors, including the differences in specific gravity and that effect on the flow, increased radiation loss for the niobium at higher temperatures, and the transient nature of the actual motion of the particles relative to the variable temperature jet. The heat transfer will depend in some measure on the relative difference between the environment temperature and the particle temperatures.

Table 3 E_m and $\rho H_m/E_m$ estimates for the six metals in this study

	E_m (J/cm^3)	$\rho H_m/E_m$
Al	2858	0.37
Cu	5985	0.30
Mo	15,016	0.27
Nb	9635	0.27
Ni	9892	0.26
Ta	11,997	0.23

As with the temperature, plots may be made of vertical velocity versus position. These plots help interpret the dynamics of the simulations. Figure 13 shows the aluminum simulation with a wide range of vertical velocities predicted for all particles in the left figure. Aluminum is by far the lowest-density metal in the analysis pool, and the particles are widely distributed around 50 m/s, with many as high as 100 m/s and many much lower, suggesting they are out of the jetting region of the plume.

This result contrasts with the tantalum particle predictions in Fig. 13 on the right. The spread is much narrower, presumably because the density of the particles helps maintain a more consistent trajectory less affected by fluctuations in the gas. There is a wide spread of velocity magnitudes, but the spread based on particle sizes is more consistent, with peak velocities of the smaller particles upward of 80 m/s, and large particles tending to be in the 30-40 m/s range. The other particle velocity results are more similar to the tantalum results than the aluminum results.

Results of the prior eight plots can be viewed differently by taking a smoothed average of the full particle distribution and plotting the average velocity and temperature. Temperatures are found plotted in Fig. 14 plotted as average absolute temperature and as normalized versus the melt temperature versus the NIST sourced melt temperatures found in Appendix. The maximum average temperatures are largely found to relate to the melt temperature, as suggested by the normalized temperature plot. The velocities plotted in Fig. 15 are roughly aligned according to particle density. Corresponding assumed values for these properties are found in Appendix.

Experimental Results

Validation of the spray predictions is a challenging prospect. The environment includes very high temperature, and sub-microsecond timescales. Prior work often omits a direct comparison between simulation predictions and experimental data, expectedly due to the challenge of obtaining data in this complex environment. Using the Accuraspray sensor, measurements of temperature and velocity were obtained. The temperatures and velocities are 3% accurate according to the manual. Experimental data provided an aleatory uncertainty in terms of a standard deviation of averaged measurements based on repeated samples. These two sources of uncertainty were presumed orthogonal and combined using the root of the sum squared for plotting. Predictions for the temperatures and velocities are presented in Fig. 12 and 13. Experimental results from the instrument with Ta powder are found in Fig. 16 and 17 plotted against simulated number averaged particle properties as a function of height. The baseline simulation result is illustrated in black, with one standard deviation of the predicted temperature or velocity illustrated with a dashed gray line above and below the black line. The standard deviation is primarily an expression of the variability occasioned by the assumed particle size distribution, which differs from the way the experimental uncertainties were derived. The data are reasonably similar to the simulation predictions, with the temperature data on the high side compared with the simulation results. Note that for the simulations the number means weight equally each particle, even those at the extremes of the distribution.
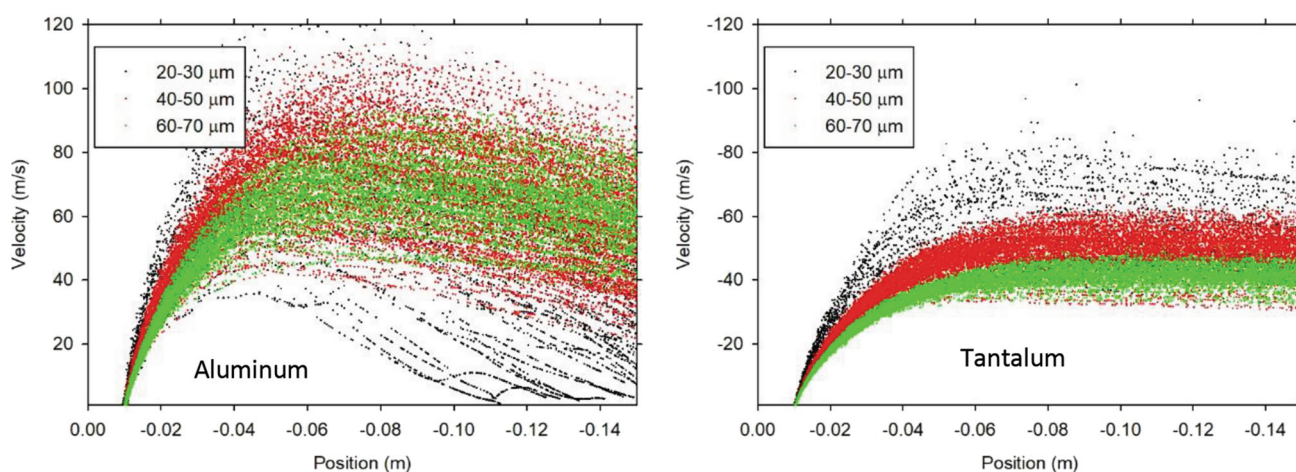

Fig. 13 Predicted particle velocity for the Al (left) and Ta (right) injection with particle sizes ranging from 20 to 30 µm (black), 40 to 50 µm (red or darker gray), and 60 to 70 µm (green or lighter gray) (Color figure online)
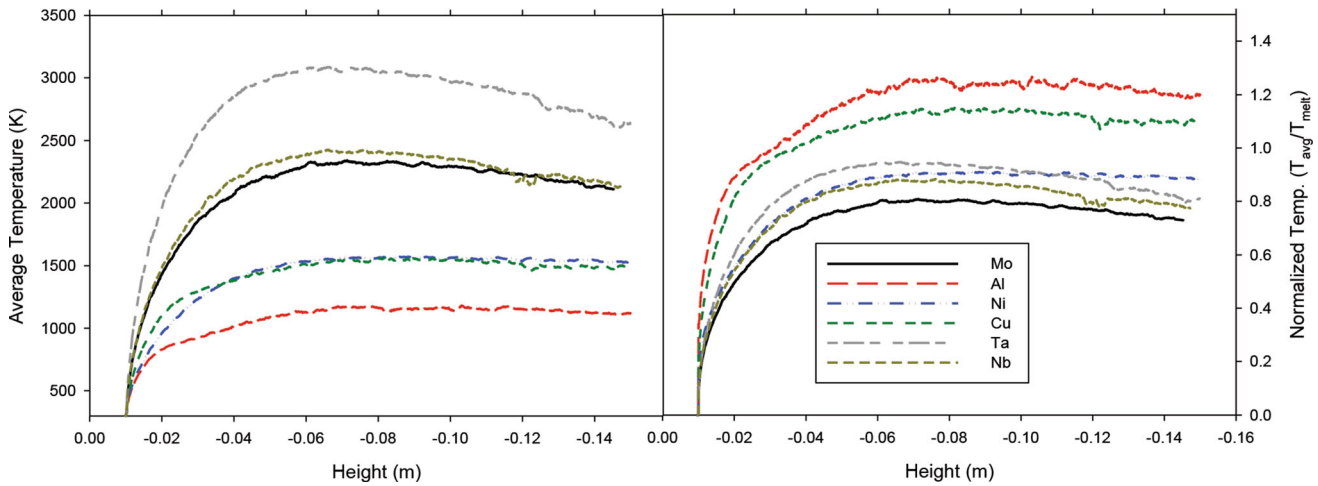
Fig. 14 Number average particle temperatures (left) and normalized temperature (right) as a function of height for the six metals
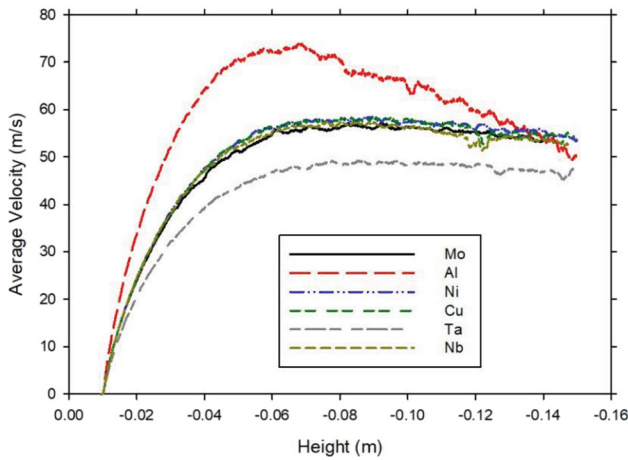

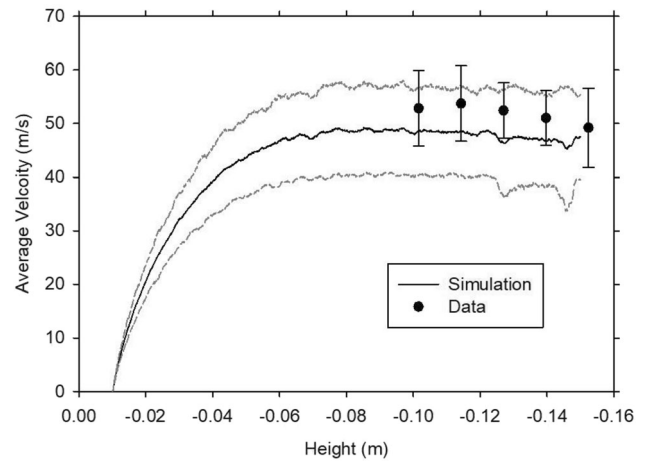**Fig. 15** Number average particle velocities as a function of height for the six metals

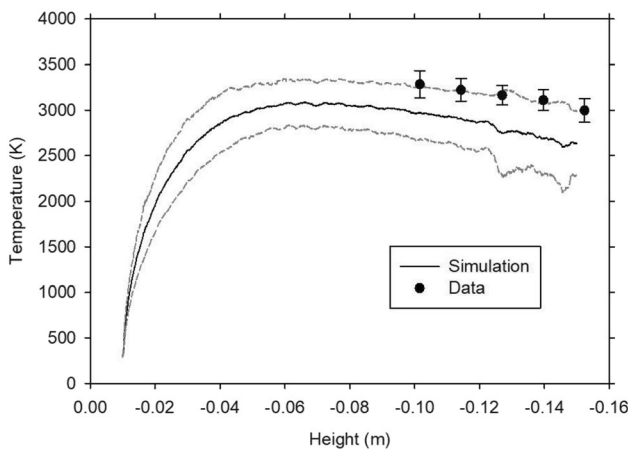**Fig. 17** Simulated number mean particle velocity vs. measurements

This is not particularly strong validation, since the data are unable to distinguish the signals by particle sizes as does the model. It is complicated by the sensitivity of the measurements to the particle size distribution which, while reasonably representative, may be significantly influenced by data coming from the difficult to match with accuracy tails of the distribution. These issues notwithstanding, the results provide a sense that the model is reasonably representative of the experimental system dynamics. The simulations and the data are sufficiently similar to proceed with the present modeling methods until better comparison or assessment methods expose critical flaws.

Model Sensitivity Factors

While evaluating meshes, it was discovered that there was a significant effect of the mesh type (i.e., hexahedral versus tetrahedral) on the inlet jet velocity. This has to do with the quality of the mesh elements in the nozzle, and the

Fig. 16 Simulated number mean particle temperature vs. measurements

resolution of the wall boundary flow therein. After exploring the sensitivity to the nozzle length, which primarily had the effect on the velocity development in the tube, the nominal length was selected to be 3.5 cm above the injection point, a full 2 cm longer than illustrated in Fig. 2. Selection was based on data comparisons, cognizant of the fact that this extended past the cathode in the nozzle design. Some of the historical modeling efforts apply simplified boundary conditions and ignore the dynamics of the nozzle when lacking MHD capability to appropriately simulate the plasma source. Our findings suggest a moderate sensitivity to input boundary conditions when approximating the nozzle with simplified LTE capabilities, and a parametric study is intended to help understand the magnitude of boundary and input condition assumptions.

In light of these sensitivity findings, a more detailed study has been made of other factors affecting model accuracy. Table 4 shows the matrix of simulation variations. Three particle size distributions were evaluated to explore the sensitivity to this factor. The particle injection tube is near the plasma jet, and of unknown temperature, likely somewhere between ambient and the melt temperature of the metal tube. The velocity of the particles was adjusted to evaluate the effect. In an effort to explore the sensitivity of the prediction to the ionization model, this was turned off with the same energy input to the injector. A case was run with the equilibrium-based ionization model, and another without, which assumed the argon flow had the same sensible energy at the injection (higher temperature), but the same energy input (without the ions), and the equilibrium rate constant was zero. This meant a higher argon inlet temperature, but no ionization. Case G explores the sensitivity of the simulations to the inlet tube length, as previously indicated having an effect on the development of the flow in the nozzle.

Figure 18 shows how the parameter variations affect the average particle temperature. The particle size distribution has a moderate effect. The inlet jet length modification Case G trends close to the baseline A case, exhibiting minor effects on the temperature. Lacking the argon ionization model results in a shift equivalent to a 5 micron average shift in the particle size distribution. The D and F

cases result in higher temperatures. This is intuitive for the D case that involves a higher initial temperature, although, the temperature difference is not the full 200 K that was added in the initial condition. The F case resulted in higher temperatures, probably due to the particles entraining better into the core hot region of the plasma jet.

The effect of the parameter study on the velocity is shown in Fig. 19. The particle size distribution has a moderate and trending effect, with larger particles reaching lower peak average velocities, as illustrated by Case A through C results. The injection velocity (Case F) has a major effect, presumably due to the particles better entraining in the core of the jet. Case G gives lower velocities. Case E results in slightly higher average particle velocities, probably because of lower densities in the injector and higher gas velocities because of the lack of ionization of the argon. Case D exhibits minimal effect on the average particle velocity. Nominal Case A results differ slightly from prior expressions of the same simulation in Fig. 16 and 17 because the particle injections were different. Even though the same distribution parameters were used, a different sampling produced minor differences in the results.

Figure 20 and 21 shows the maximum average particle temperatures and velocities extracted from the simulation
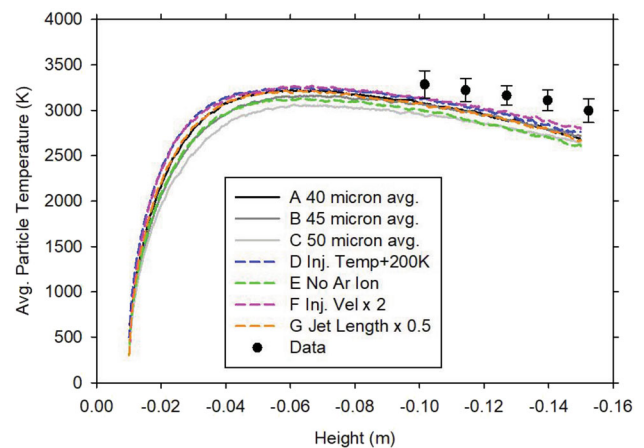
Fig. 18 The effect of various parameters on the predicted average particle temperature

Table 4 Sensitivity analysis parameters

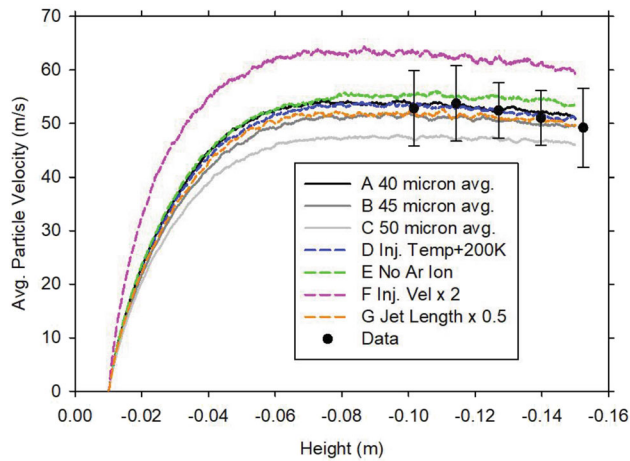| Case	lambda	Mean particle size, micron	Other
A	43	40	
B	48	45	
C	53	50	
D	43	40	Particle injection temperature 200 K above ambient
E	43	40	No argon ionization model
F	43	40	Particle injection velocity × 2
G	43	40	Main inlet 50% shorter

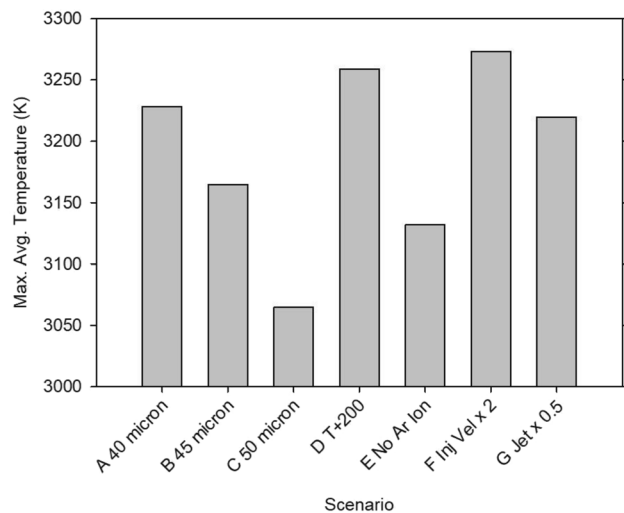**Fig. 19** The effect of various parameters on the predicted average particle velocity

Fig. 20 Maximum of the average particle temperature for the parameter variations

Fig. 21 Maximum of the average particle velocity for the parameter variations

Discussion

The largely empirically based determination of injection conditions for experimental plasma spray application of metal coatings is a potentially cumbersome approach to a difficult problem. Modeling adds a tool that can help interpret or obtain guidance that can help shorten what would otherwise be a more involved process approached only with experimental tools. Its utility is contingent on its accuracy, and the components of the model that lend to accurate predictions. This effort has explored a number of relatively unexplored features of model accuracy in prior studies. The material properties for the metals in this study were not found to be easily obtained, with increasing variability in higher-temperature properties and in the rarer metals. The suitable conditions for a deposition are ultimately determined by the quality of the deposition. This depends on the particles being in a melt condition, and also the spray not causing the target material to melt or decompose. With numerous open parameters including the injector power, flow rates, and particle size distributions, it is challenging to develop a consistent and ideal set of conditions for application.

Verification and validation processes add confidence and credibility to the simulation efforts. Verification is a fundamental activity whereby the modeling is deemed to be correctly coded and representative of the physical models as intended. This is largely provided by historical testing, and nightly regression testing of version-controlled software. Verification also involves solution verification. The mesh adequacy evaluation shown here suggests simulations are in a reasonably convergent regime. Validation is more challenging because the historical studies involving prior

predictions in Fig. 18 and 19. These compliment the prior plots by providing a more direct way of comparing across individual calculations in the matrix. For parameters varied, the maximum average temperature had a range of about 250 K, whereas the maximum average velocity varied within a range of about 15 m/s. These suggest parametric modeling uncertainties evaluated, and particle size distribution uncertainties have a moderate effect on the resultant particle velocities and temperatures. Significantly, Cases D through G, which are one-off cases from Case A, exhibit at the least about 50 K difference from the baseline. On this basis, we conclude that the effect of these parameters is moderate, and that they are important considerations when attempting to model a system of this nature.
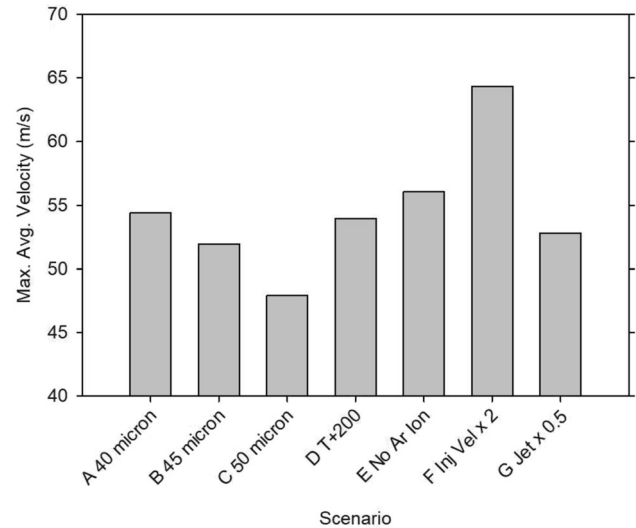
validation are in many cases far enough removed from this applications space to demand further exploration of model accuracy. The test comparisons illustrated herein are a good step in the right direction for this application. They illustrate that for given settings the nominal simulations match the data to within a standard deviation of the particle predictions. This is good, but not a particularly high achievement, as the bounds are wide due to the particle size distribution range. The modeled distribution may be reasonably representative of the test, but the average particle dynamics will be most sensitive to the large and small particles at either end of the distribution, which vary the greatest from the average. Small errors in these could result in significant shifts in the average because the particles on the extreme sides of the distribution give the most extreme velocity and temperature magnitudes. Improved validation will require either a more carefully controlled particle size distribution, or a more selective diagnostic. Note that the measured and modeled distributions shown in Fig. 8 and 9 differ moderately in the low particle size range.

A validation challenge continues to be obtaining good comparison data. Detailed experimental studies like that of Mauer et al. (Ref 43) provide high-fidelity data suitable for comparisons. But there are a variety of nozzles, power settings, gases, particles, and flow rates of interest. There is a continuing need for data across a broader range of test conditions to help improve model validation for the variety of applications of interest to the plasma spray community. The data presented herein help contribute to this need, although the precise interpretation of the temperature data and how to weight the mean value based on the particle size distribution involves some challenging uncertainties. This includes the unknown variable distribution of the particles in the sampling volume, the sensitivity factor of the measure to the particle fines, and the weighting factor of the signal to the particle sizes. The number averaged simulations from a few similar distributions with varying means suggests a moderate effect of this factor on the magnitude of the extracted temperature, which expresses the variability that may also be present in the measurements depending on the uncertainties.

There are a number of aspects of the model that are understood to be lacking, which may have an effect on the quantitative accuracy of the simulations. Formerly acknowledged and previously studied in the literature are the equilibrium plasma model, the radiation model, turbulence model, and the uniform particle temperature assumption. We are also assuming non-spherical particles are behaving like spheres, which is a common assumption in this particle regime. All these issues notwithstanding, we have produced simulations that compare favorably on the particle temperatures with the measurements with the suite of physics models employed. Measured particle velocities are moderately higher than the simulated values, but sensitivity to a few of the inlet parameters and the range of the variance due to the distribution is well able to account for the discrepancy. Likewise, the average predicted particle temperatures tend to be predicted a little below the measurements. Parameter uncertainty can also be attributed to the variations in velocity and temperature trends with height. Significantly, both parameters trend about the same, with the downward slope indicating a relatively consistent lapse rate for both parameters. This suggests the momentum and heat loss characteristics are reasonably well captured in the jet, and the gas velocities and temperatures are in a reasonable range. The parameter study suggests that the deviation from mean can be easily accounted for in input parameter uncertainties, as well as possibly some of the aforementioned modeling approximations. Qualitative assessments with computational tools of this nature are thought to be reasonably representative and valuable because the ability to measure in this environment is challenging. Quantitative accuracy will continue to be challenged by uncertainties in the input conditions and model forms employed, with an increased ability to better characterize the input conditions helping to improve aspects of the comparison.

The equilibrium modeling method described here is in the same class as the LTE approximations employed by others. We avoid a call to an equilibrium model during code operation by fitting the relation for the ionization model to a temperature-based function. A relatively simple model form resulted in a very good fit, making this an attractive and possibly more cost-effective way of addressing the ion dynamics of the gases than repeated calls to an equilibrium code. In the sensitivity study, the use of the equilibrium model exhibited a moderate effect on the results. Considering that the torch power setting was relatively low for this scenario, we avoid concluding that the ionization model is of marginal importance. At higher settings, it is anticipated that it will be of increasing importance. This method combines well with this application because our light gas (He) does not ionize significantly until much higher temperatures. This would probably not work as well for the more commonly deployed gas jets such as Ar/H_2 without adaptation, as H_2 ionizes more readily than the Ar. The merits of developing a full ionization model include improved confidence in the results for a range of conditions and gases, however, this comes with a cost. It would be a helpful exercise to assess the magnitude of the effect. Such an activity would require a code or platform with both capabilities. It would help identify and quantify regimes where the LTE model is an increasingly poor assumption and guide the application use of the different approaches to the ionization problem in plasma spray models.

LTE has been used inside an SG-100 injector recently, as described by Dalir et al. (Ref 6-8), although accommodations were made for the plasma arc modeling to achieve reported results.

Another differentiating feature of this study is the evaluation of a number of different spray particle types. The results show that depending on the metal being injected that the spray characteristics need to be adjusted to achieve a more optimal result of the majority of the particles being in the melt regime without an untenably high ambient gas temperature. A few constructs are presented to help guide development of application processes. It was generally found that the particle dynamics were functional to one primary material property. Cognizance of this relationship can help more quickly obtain a suitable condition for deposit application purposes when transitioning to new metals.

This work identifies some points of emphasis regarding simulations of this type given what has been traditionally noted as factors in the accuracy of the predictions. We have shown for our model that the inflow boundary condition can have a moderate effect on the outcome of the spray. Merely extending the mesh further into the injector produces a different flow profile, and results in moderate changes to the particle behavior. We further show evidence that the details regarding the injection of the particles within a practical range of approximation may also have an effect on the dynamics of the spray. The particle properties have effects on the outcome of the simulations, and there are instances noted where the source materials differ greatly in their magnitudes, and where uncertainties are comparatively large. It is attractive to assume that the plasma dynamics in the nozzle can be abstracted by a boundary condition to simulate the jet and particle spray dynamics. The alternative adds significant computational expense to what is already a challenging flow problem. Even without the plasma dynamics in the nozzle, our time steps were on the order of a microsecond, and full simulation times seldom exceeded 100 ms due to computation costs. Applications to parts typically involve significantly longer spray exposures. It may be insightful at some point to assess the full fluid mechanical and heat transport dynamics of an application process to help guide the procedures. Despite lacking the added complexity of an ionization model, such a computation will still demand significant computational resources to the point of being questionably viable without major computational speed improvements.

Conclusions

A modeling technique for Ar/He plasma spray metal coatings is presented that provides a unique approach to the plasma problem with performance comparable to the common LTE assumption made for the majority of the historical simulations of this nature. A 3D hybrid LES/RANS technique with evaporating particles was used to evaluate the dynamics of the spray drops as a function of vertical release distance for a suite of metals. Metal properties were evaluated from multiple sources with a range of agreement, suggesting the value of the exercise and the potential need for confirmatory property data in the high-temperature regime. Predictions for six metals are illustrated for a single flow condition. The effect of particle size suggests a range of results highly dependent on the size distribution, but also dependent on the dynamics of the flow and boundary conditions within a range of uncertainty for the process. Material type also contributes to a significant variation in performance and using a more simple numerical approximation for the energy required to achieve melt appears to largely follow the performance as predicted by the more detailed model. Incipient validation work is described, with the dataset comparing to the simulations favorably for this application scenario.

Appendix 1: Details on the Ionization Model

To use the equilibrium data in the code, an empirical function was fit to the TIGER data. This provided a simple means to access the equilibrium concentrations without having to resort to a call to the equilibrium calculator every time a value was needed. Two initial models were first explored employing the error function and the hyperbolic tangent functions:

$$f(T) = 0.5 + 0.5 * \tan h\left(\frac{T}{C1} - C2\right)$$

$$f(T) = 0.5 + 0.5 * \operatorname{erf}\left(\frac{T}{C1} - C2\right).$$

A parameter regression fit was used to generate fits, and the error (difference squared) was evaluated for each of the fits as a function of temperature. The errors are plotted in Fig. 22.
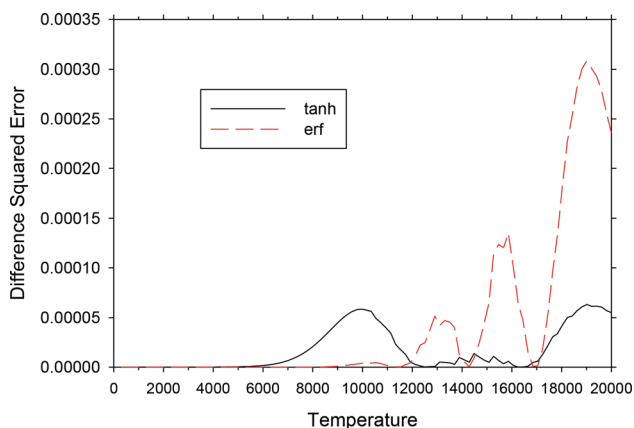
Fig. 22 Model fit error for the two baseline models fit to TIGER equilibrium predictions

Fig. 23 The error plot for the tanh-Gaussian model plotted on the same scale as the tanh and erf models

The error for the model using the error function is mostly at the higher temperatures, which in preliminary scoping were not found to be prevalent in the plasma sprays we were simulating. The hyperbolic tangent function gave two main error peaks, one at 10,000 K and the other at around 19,000 K. The lower temperature peak was of interest to reduce. The shape of the error is close to a Gaussian shape, so a term of this nature was added to the fit to reduce that error:

$$f(T) = 0.5 + 0.5 * \tan h\left(\frac{T}{C1} - C2\right)$$
$$- C5/\left(C4\sqrt{2\pi}\right)\exp\left(-0.5 * \left((T - C3)/C4\right)^2\right).$$

This added term resulted in the error found in Fig. 23, a much lower error in the range of interest. The error is plotted on a similar scale as the previous plot to aid in comparisons.

It was also thought to be prudent to look at altering the range of the data fit to focus on the regime where the model is actually going to be applied. This was considered 12,000 K and below based on early simulations of a number of test conditions. Two additional fits were generated using the tanh and erf functions that focused the fit on achieving highest accuracy in this narrower temperature range. Table 5 summarizes the five fits considered for this study. The range considered for the fit as well as the best fit constants is shown.

The fit was performed at the temperature intervals produced by TIGER. At these intervals, the error was calculated (as plotted in the prior 3 figures) and summed. The error is found plotted in Fig. 24. There are two different error terms for each fit. One includes the data up to 12,000 K, and the other the full range of data up to 20,000 K. Just considering the 12,000 K range, the erf1 model performed superior to the others, with a summed
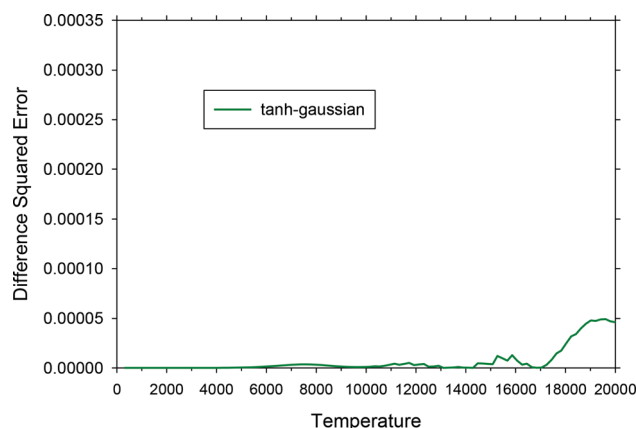
error at least an order of magnitude lower than the others. If, however, the full 20,000 K range of accuracy is required, the tanh-Gaussian fit is slightly better than the next closest, which is the tanh1 fit.

The decision on which fit to use includes an additional set of factors. These functions are moderately complex numerical functions. It is desirable to have the function not adversely affect the speed of the calculations. The tanh and erf functions were relatively equivalent in impact on the rate of turn-around of similar jobs during testing. The tanh-Gaussian fit was noticeably slower (abt. 10-20%). This assessment should not be considered definitive, as the jobs were run on clusters that can go through periods of over-subscription and variable loading on the CPUs as well as the communication data streams. A more definitive assessment might be desirable in the future and would need to be done in a more sterile computational environment. The results found make sense, however, as the Gaussian term requires extra compute power to calculate the additional terms.

Evaluating some preliminary results for conformance to equilibrium, relatively few points in the domain experienced plasma concentrations significantly out of equilibrium, with the vast majority of these being at high elevations (in and near the nozzle). This is illustrated in Fig. 25 and 26, taken from a sampling of nodal concentration and temperatures on a plane in the domain of a spray simulation. The nozzle exit was at zero cm, and the scenario injected 10,000 K argon gas (20 LPM). Here the temperature function was the 'erf1' model. There are points where the predicted ion fraction is significantly different from the model, however these tend to be close to the injector (< 2.5 cm). These are a minority, and most of the data at an inch or below the nozzle are within a few percent of the model equilibrium values. This suggests that the equilibrium assumption is mostly valid below the nozzle,

Table 5 Details for the five argon ionization fits

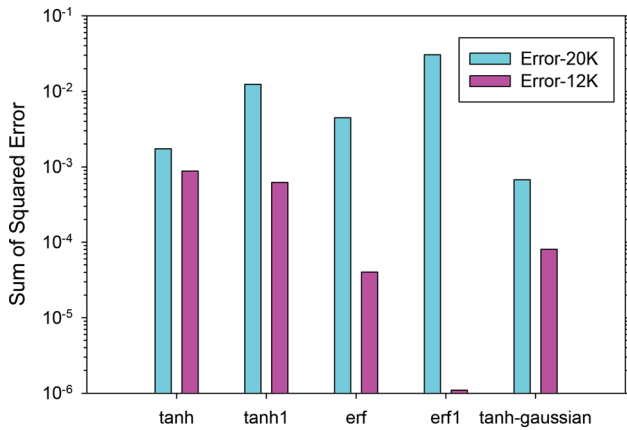| Model	Range	C1	C2	C3	C4	C5
tanh	02–e4 K	2574.76	5.65120			
tanh1	0–1.2e4 K	2474.0	5.83417			
Erf	0–2e4 K	3039.29	4.70406			
erf1	0–1.2e4 K	3277.00	4.49620			
tanh-Gaussian	0–2e4 K	2605.25	5.28208	10,040.2	1500.3	30

Fig. 24 Error summation from the various argon ion models for two temperature ranges
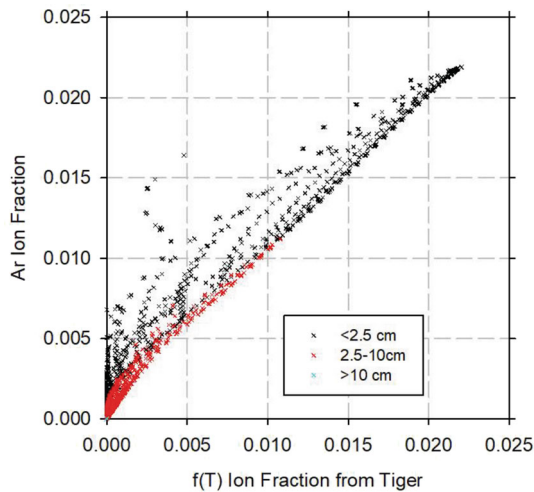

Fig. 25 A comparison of the present model predictions to the equilibrium function fit to the TIGER model

and the non-equilibrium predictions are most prevalent in the dynamic region closest the nozzle.

This equilibrium model has the positive features of not being a significant computational burden, being based on verified data, retaining the property of being energy conservative, and having flexibility to function robustly in a CFD environment that includes energy and species transport equations. Potential issues with the model include lack of non-equilibrium capabilities, lag in the equilibrium (of
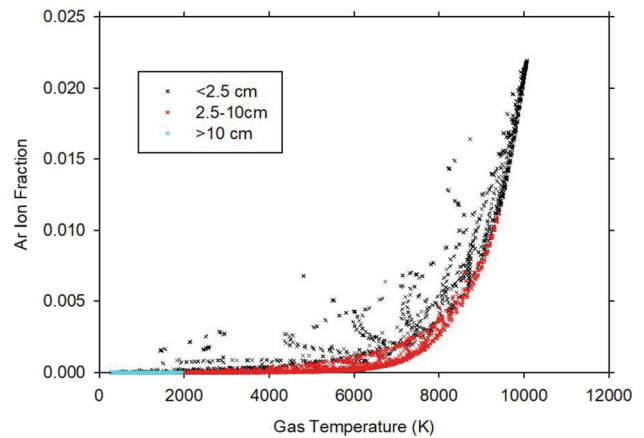

Fig. 26 Plasma torch equilibrium test Illustrating predicted temperature relationship with Ar ion fraction at various ranges of distance below the injector

somewhat arbitrary nature), some residual error in the empirical model, and a dependency on the accuracy of the TIGER equilibrium predictions.

Appendix 2: Material Property Details

As mentioned in the body of the report, an effort was made to identify all properties with multiple sources to help establish the agreement among the various reports. This exercise was instructive, and when agreement was lacking helps identify need for additional measurements or assessments to improve the accuracy of the reference figure. Table 6 shows boiling temperatures, which were generally in agreement, but had for Ni a standard deviation as high as about 100 for the three sources for the characteristic temperature.

Melting temperatures were considerably more uniform among the different sources, as shown in Table 7. The largest standard deviation was for Ta, only 15° with the average at 3272 K.

Heat of fusion is the latent heat for the phase change between liquid and solid and was found in multiple sources. The agreement was poorest for Mo and Ta, as indicated by Table 8. In the case of Mo, there was a single outlier with the other two in agreement. For Ta, the three values were all

Table 6 Boiling temperatures from three sources in Kelvin

Species	Smithell Tboil, K	NIST Tboil, K	CRC/efunda Tboil, K	Avg	St. dev
Al	2793	2790.8	2740	2774.6	29.99
Cu	2833	2843.0	2835	2837.0	5.29
Mo	4883	4952.0	4912	4915.7	34.63
Nb	5013	5130.8	5015	5052.9	67.46
Ni	3183	3156.6	3005	3114.9	96.06
Ta	5643	5778.1	5698	5706.4	67.92

Table 7 Melt temperatures for six metals from three sources in Kelvin

Species	Smithell Tmelt, K	NIST Tmelt, K	CRC/efunda Tmelt, K	Avg	St. dev
Al	933.1	933.5	933.4	933.3	0.18
Cu	1356	1358	1358	1357.3	0.84
Mo	2893	2896	2896	2895.0	1.73
Nb	2740	2750	2741	2743.7	5.51
Ni	1726	1728	1726	1726.7	1.15
Ta	3288	3258	3269	3271.7	15.18

Table 8 Heat of fusion (kJ/kg) from three sources

Species	Smithell, kJ/kg	NIST, kJ/kg	Engineering toolbox, kJ/kg	Avg	St. dev
Al	388.0	391.4	396	391.81	4.00
Cu	204.9	186.6	206	199.18	10.87
Mo	371.0	433.2	375	393.06	34.82
Nb	315.4	319.1	288	307.50	17.00
Ni	292.4	297.8	293	294.40	2.98
Ta	136.5	170.2	199	168.57	31.28

Table 9 Ambient specific gravity (SG), atomic weight (AW), and heats of evaporation

Species	SG	AW	Smithell, kJ/kg	Periodic table, kJ/kg	Avg	St. dev
Al	2.70	26.98	10,781.45	10,859.28	10,820.36	55.03
Cu	8.96	63.55	4796.53	4720.99	4758.76	53.41
Mo	10.20	95.94	6151.52	6253.91	6202.71	72.40
Nb	8.57	92.91	7359.02	7426.83	7392.93	47.95
Ni	8.90	58.71	6377.21	6438.45	6407.82	43.29
Ta	16.7	180.95	4324.45	4067.47	4195.96	181.71

different. In the case of Ta, the standard deviation was significantly greater than 10% of the average.

The heat of evaporation is the latent heat for the phase transition between liquid to gas. Two sources listed this property, and the two sources were largely in agreement, as suggested by Table 9. Also included in this table are the specific gravity (SG) at ambient conditions, and the atomic weight (AW), which did not exhibit significant variability in the resources.

Reported digits in Appendix tables are not intended to convey physical accuracy, rather, are meant to convey computed accuracy based on unit conversions and transcriptions. All results are reported to consistent levels of numeric accuracy. Source documentation should be consulted for property accuracy information, which as the statistical measures suggest is not nearly as high as the reported digits in the tables. A single source was found for the critical temperature, which is used in the particle model for predicting the rate of evaporation. This was the efunda website, for which data were extracted in 2020. These are not repeated here, as they are expected to remain available on the website.

Appendix 3: Selected Governing Equations

The simulations involve CFD predictions, which are governed by the Navier–Stokes equations with segregated solves for continuity, momentum, energy, species, and turbulent parameters.

The continuity equation using conventional notation for j coordinates is:

$$\frac{\partial \rho}{\partial t} + \frac{pu_j}{\partial x_j} = S_m. \tag{Eq C − 1}$$

The i momentum equations are:

$$\frac{\partial(pu_i)}{\partial t} + \frac{\partial(pu_i u_i)}{\partial x_i} + \frac{\partial p}{\partial x_i} = \frac{\partial T_{ij}}{\partial x_j} + pg_i + S_{ui}. \tag{Eq C − 2}$$

The energy equation is:

$$\frac{\partial(ph)}{\partial t} + \frac{\partial\left(phu_j\right)}{\partial x_j} = \frac{\partial}{\partial x_j}\left(k\frac{\partial T}{\partial x_j}\right) - \frac{\partial}{\partial x_j}\left(\sum_k ph_k Y_k \hat{u}_{j,k}\right) + S_n \tag{Eq C − 3}$$

here $\hat{u}$ is the diffusion velocity. The species equations for k species are:

$$\frac{\partial(pY_k)}{\partial t} + \frac{\partial\left(pY_k u_j\right)}{\partial x_j} = \frac{\partial\left(pY_k \hat{u}_{j,k}\right)}{\partial x_j} + p\dot{\omega}_k + S_{Yk}. \tag{Eq C − 4}$$

The Lagrangian–Eulerian coupling involves computation of the transport of spherical particles, with the momentum transport dictated by:

$$\frac{du_{p,i}}{dt} = \frac{3p_g C_D \left|\overrightarrow{u_g} - \overrightarrow{u_p}\right|}{4p_p d_p}\left(u_{g,i} - u_{p,i}\right) + \left(\frac{p_p - p_g}{p_p}\right)g_i. \tag{Eq C − 5}$$

The particle evaporation and heating model is based on film theory for a spherical particle with empirical corrections to account for non-spherical effects from particle slip. The particle enthalpy and evaporation are governed by the mass loss rate. For equal Prandtl and Schmidt numbers, evaporation can use thermal or mass diffusion transport properties interchangeably (ρD for k/Cp), and the Nusselt diffusion-based evaporation rate following the classical Spalding transfer number approach is:

$$\dot{m} = 4\pi p r_p (pD)_{\text{eff}}\frac{\text{Sh}_f}{\text{Sh}_{f,\text{Re}=o}}\ln(1 + B) \tag{Eq C − 6}$$

where

$$\frac{\text{Sh}_f}{\text{Sh}_{f,\text{Re}=0}} = \left(1 + 0.3\,\text{Re}^{1/2}\text{Sc}^{1/3}\right) \tag{Eq C − 7}$$

and B is the Spalding transport number:

$$B = \frac{Y_f - Y_\infty}{Y_p - Y_f} \tag{Eq C − 8}$$

here Y_f is the film mass fraction, Y_p is the particle mass fraction (1 for single component particles), and Y_∞ is the free-stream mass fraction. The film mass fraction may be deduced from the film partial pressure from the Clausius–Clapeyron relation:

$$P_F = P_{\text{ref}}\exp\left[h_{\text{vap}}\frac{MW}{R}\left(\frac{1}{T_{\text{ref}}} - \frac{1}{T_p}\right)\right] \tag{Eq C − 9}$$

here h_{vap} is the enthalpy of vaporization and P_{ref} is the vapor pressure at T_{ref}.

To find the particle heating rate, it is recognized that the Spalding transport number in Eq C-8 can be written in terms of the mass transport or in terms of related heat transfer and these two expressions are equal:

$$\frac{\dot{m}C_p(T_f - T_\infty)}{\dot{m}h_{\text{vap}} + Q_{\text{rad}} + m_p C_p \frac{dT_p}{dt}} = B = \frac{Y_f - Y_\infty}{Y_p - Y_f} \tag{Eq C − 10}$$

here m_p and C_p are the particle mass and specific heat while $Q_{\text{rad}} = 4\pi r^2(\sigma T^4 - G_{\text{in}}/4)$ is the radiative heat transfer to the particles. For the radiative heat transfer, G_{in} is the incident radiation intensity (integrated over all directions), α is the particle emissivity and σ is the Stefan–Boltzmann constant. Using the right-hand side of Eq C-6 for $\dot{m}$ the Spalding transfer number in terms of the heat transfer components can be solved for the particle heating rate:

$$m_p C_{v,p}\frac{dT_p}{dt} = \frac{\dot{m}c_p(T_f - T_\infty)}{B} - \dot{m}h_{\text{vap}} - Q_{\text{rad}}. \tag{Eq C − 11}$$

The particle equations are sub-stepped for each Eulerian step, and the source/sink terms for the Eulerian equations are accumulated and passed to the gas-phase fluid solver where they are implemented as source terms (S) added to the right-hand side of the unit consistent and appropriate gas-phase transport equations listed above (Eq C-1 through C-4).

References

1. C.H. Chang and J.D. Ramshaw, Numerical Simulation of Nonequilibrium Effects in an Argon Plasma Jet, *Phys. Plasmas*, 1994, **1**(11), p 3698-3708.

2. I. Ahmed and T.L. Bergman, Optimization of Plasma Spray Processing Parameters for Deposition of Nanostructured Powders for Coating Formation, *J. Fluids Eng.*, 2006, **128**, p 394-401.

3. R.L. Williamson, J.R. Fincke and C.H. Chang, A Computational Examination of the Sources of Statistical Variance In Particle Parameters During Thermal Plasma Spraying, *Plasma Chem. Plasma Process.*, 2000, **20**(3), p 299-324.

4. R.L. Williamson, J.R. Fincke, D.M. Crawford, S.C. Snyder, W.D. Swank and D.C. Haggard, Entrainment in High-Velocity, High-Temperature Plasma Jets: Part II: Computational Results and Comparison to Experiment, *Int. J. Heat Mass Transfer*, 2003, **46**(22), p 4215-4228.

5. H.B. Xiong, L.L. Zheng, S. Sampath, R.L. Williamson and J.R. Fincke, Three- Dimensional Simulation Of Plasma Spray: Effects of Carrier Gas Flow and Particle Injection on Plasma Jet and Entrained Particle Behavior, *Int. J. Heat Mass Transf.*, 2004, **47**(24), p 5189-5200.

6. E. Dalir, A. Dolatabadi and J. Mostaghimi, Modeling of Suspension Plasma Spraying Process Including Arc Movement Inside the Torch, *J. Therm. Spray Technol.*, 2019, **28**(6), p 1105-1125.

7. E. Dalir, A. Dolatabadi and J. Mostaghimi, Modeling the Effect of Droplet Shape and Solid Concentration on the Suspension Plasma Spraying, *Int. J. Heat Mass Transf.*, 2020, **161**, p 120317.

8. E. Dalir, A. Dolatabadi and J. Mostaghimi, Investigating the In-flight Droplets' Atomization in Suspension Plasma-Sprayed Coating, *Int. J. Heat Mass Transf.*, 2022, **182**, p 121969.

9. G. Delluc, H. Ageorges, B. Pateyron, P. Fauchais, Fast Modelling of Plasma Jet and Particle Behaviours in Spray Conditions. High Temp. Mater. Proc. Int. Q. High-Technol. Plasma Process. **9**(2) (2005)

10. F. Jabbari, M. Jadidi, R. Wuthrich and A. Dolatabadi, A Numerical Study of Suspension Injection in Plasma-Spraying Process, *J. Therm. Spray Technol.*, 2014, **23**(1–2), p 3-13.

11. M. Jadidi, M. Mousavi, S. Moghtadernejad and A. Dolatabadi, A Three-Dimensional Analysis of the Suspension Plasma Spray Impinging on a Flat Substrate, *J. Therm. Spray Technol.*, 2015, **24**(1–2), p 11-23.

12. K. Remesh, S.C.M. Yu, H.W. Ng and C.C. Berndt, Computational Study and Experimental Comparison of the In-flight Particle Behavior for an External Injection Plasma Spray Process, *J. Therm. Spray Technol.*, 2003, **12**(4), p 508-522.

13. K. Remesh, H.W. Ng and S.C.M. Yu, Influence of Process Parameters on the Deposition Footprint in Plasma-Spray Coating, *J. Therm. Spray Technol.*, 2003, **12**(3), p 377-392.

14. C.W. Kang, H.W. Ng and S.C.M. Yu, Comparative Study of Plasma Spray Flow Fields and Particle Behavior Near to Flat Inclined Substrates, *Plasma Chem. Plasma Process.*, 2006, **26**(2), p 149-175.

15. C.W. Kang, H.W. Ng and S.C.M. Yu, Plasma Spray Deposition on Inclined Substrates: Simulations and Experiments, *J. Therm. Spray Technol.*, 2007, **16**(2), p 261-274.

16. A.F. Kanta, M.P. Planche, G. Montavon and C. Coddet, In-flight and Upon Impact Particle Characteristics Modelling in Plasma Spray Process, *Surf. Coat. Technol.*, 2010, **204**(9–10), p 1542-1548.

17. M.Y. Kharlamov, I.V. Krivtsun, V.N. Korzhyk, Y.V. Ryabovolyk and O.I. Demyanov, Simulation of motion, heating, and breakup of molten metal droplets in the plasma jet at plasma-arc spraying, *J. Therm. Spray Technol.*, 2015, **24**(4), p 659-670.

18. E. Meillot, D. Guenadou and C. Bourgeois, Three-dimension and Transient DC Plasma Flow Modeling, *Plasma Chem. Plasma Process.*, 2008, **28**(1), p 69-84.

19. E. Meillot, S. Vincent, C. Caruyer, J.P. Caltagirone and D. Damiani, From DC Time- Dependent Thermal Plasma Generation to Suspension Plasma-Spraying Interactions, *J. Therm. Spray Technol.*, 2009, **18**(5), p 875-886.

20. E. Meillot, S. Vincent, C. LeBot, F. Sarret, J.P. Caltagirone and L. Bianchi, Numerical Simulation of Unsteady ArH2 Plasma Spray Impact on a Moving Substrate, *Surf. Coat. Technol.*, 2015, **268**, p 257-265.

21. K. Pourang, C. Moreau and A. Dolatabadi, Effect of Substrate and its Shape on In-flight Particle Characteristics in Suspension Plasma Spraying, *J. Therm. Spray Technol.*, 2016, **25**(1–2), p 44-54.

22. P. Fauchais and A. Vardelle, Thermal Plasmas, *IEEE Trans. Plasma Sci.*, 1997, **25**, p 1258-1280.

23. P. Fauchais and A. Vardelle, Heat, Mass and Momentum Transfer in Coating Formation by Plasma Spraying, *Int. J. Therm. Sci.*, 2000, **39**(9–11), p 852-870.

24. A.B. Murphy, Transport Coefficients of Helium and Argon-Helium Plasmas, *IEEE Trans. Plasma Sci.*, 1997, **25**(5), p 809-814.

25. A.B. Murphy, Transport Coefficients of Hydrogen and Argon–Hydrogen Plasmas, *Plasma Chem. Plasma Process.*, 2000, **20**(3), p 279-297.

26. A.B. Murphy and D. Uhrlandt, Foundations of High-Pressure Thermal Plasmas, *Plasma Sources Sci. Technol.*, 2018, **27**(6), p 063001.

27. S.M. Modirkhazeni and J.P. Trelles, Non-transferred Arc Torch Simulation by a Non- equilibrium Plasma Laminar-to-Turbulent Flow Model, *J. Therm. Spray Technol.*, 2018, **27**(8), p 1447-1464.

28. A. Lebouvier, C. Delalondre, F. Fresnet, V. Boch, V. Rohani, F. Cauneau and L. Fulcheri, Three-dimensional Unsteady MHD Modeling of a Low-current High-voltage Nontransferred DC Plasma Torch Operating with Air, *IEEE Trans. Plasma Sci.*, 2011, **39**(9), p 1889-1899.

29. C. Chazelas, J.P. Trelles and A. Vardelle, The Main Issues to Address in Modeling Plasma Spray Torch Operation, *J. Therm. Spray Technol.*, 2017, **26**(1–2), p 3-11.

30. A. Kaminska, B. Lopez, B. Izrar and M. Dudeck, Modelling of an Argon Plasma Jet Generated by a dc Arc, *Plasma Sources Sci. Technol.*, 2008, **17**(3), p 035018.

31. SIERRA Thermal/Fluid Development Team, SIERRA Low Mach Module: Fuego Theory Manual," SAND2019-12289

32. SIERRA Thermal/Fluid Development Team, "SIERRA Low Mach Module: Fuego User Manual," SAND2019-12291.

33. S.R. Tieszen, S.P. Domino, A.R. Black, Validation of a Simple Turbulence Model Suitable for Closure of Temporally-Filtered Navier-Stokes Equations Using a Helium Plume. SAND2005-3210, June 2005, Sandia National Laboratories

34. W.A. Sirignano, *Fluid Dynamics and Transport of Droplets and Sprays*, Cambridge University Press, Cambridge, UK, 1999.

35. M. Vardelle, A. Vardelle and P. Fauchais, Spray Parameters and Particle Behavior Relationships During Plasma Spraying, *J. Therm. Spray Technol.*, 1993, **2**(1), p 79-91.

36. M.I. Boulos, P. Fauchais and E. Pfender, *Thermal Plasmas: Fundamentals and Applications*, Springer, LLC, New York, 1994.

37. M.L. Hobbs, K. Tanaka, M. Iida, T. Matsunaga, Equilibrium calculations of firework mixtures. In *3rd (Beijing) International Symposium on Pyrotechnics and Explosives, Beijing, China*, (1995).

38. T.M. Rodgers, J.A. Mitchell, A. Olson, D.S. Bolintineanu, A. Vackel and N.W. Moore, Fast Three-Dimensional Rules-Based Simulation of Thermal-Sprayed Microstructures, *Comput. Mater. Sci.*, 2021, **194**, p 110437.

39. C.T. Lynch, R. Summitt, and A. Sliker Eds., *CRC Handbook of Materials Science*, Vol 1 CRC Press, Boca Raton, 1974

40. J.J. Valencia, P.N. Quested, *Thermophysical Properties ASM Handbook, Volume 15: Casting ASM Handbook Committee* (2008), pp. 468-481

41. E.A. Brandes and G.B. Brook Eds., *Smithells Metals Reference Book*, Elsevier, Amsterdam, 2013

42. R. Hultgren, P.D. Desai, D.T. Hawkins, M. Gleiser, K.K. Kelley and D.D. Wagman, *Selected Values of the thermodynamic Properties of the Elements*, American Society for Metals, Metals Park, Ohio, USA, 1973.

43. G. Mauer, R. Vaßen, D. Stöver, S. Kirner, J.L. Marqués, S. Zimmermann, G. Forster and J. Schein, Improving powder injection in plasma spraying by optical diagnostics of the plasma and particle characterization, *J. Therm. Spray Technol.*, 2011, **20**(1–2), p 3-11.